

Interpretation of thermal emission. I. The effect of roughness for spatially resolved atmosphereless bodies



Björn J.R. Davidsson^{a,*}, Hans Rickman^{a,b}, Joshua L. Bandfield^{c,1}, Olivier Groussin^{d,2}, Pedro J. Gutiérrez^{e,3}, Magdalena Wilska^b, Maria Teresa Capria^{f,4}, Joshua P. Emery^{g,5}, Jörn Helbert^h, Laurent Jorda^{d,2}, Alessandro Maturilli^{h,6}, Thomas G. Mueller^{i,7}

^a Department of Physics and Astronomy, Uppsala University, Box 516, SE-75120 Uppsala, Sweden

^b PAN Space Research Center, Bartycza 18A, PL-00716 Warsaw, Poland

^c Space Science Institute, 4750 Walnut St. Suite 205, Boulder, CO 80301, USA

^d Aix Marseille Université, CNRS, LAM (Laboratoire d'Astrophysique de Marseille) UMR 7326, 13388 Marseille, France

^e Instituto de Astrofísica de Andalucía-CSIC, Aptd. 3004, 18080 Granada, Spain

^f INAF-IASF, Via del Fosso del Cavaliere 100, 00133 Roma, Italy

^g Earth and Planetary Sciences, University of Tennessee, 306 Earth and Planetary Sciences Building, Knoxville, TN 37996-1410, USA

^h Deutsches Zentrum für Luft- und Raumfahrt e.V. in der Helmholtz-Gemeinschaft, Berlin-Adlershof, Rutherfordstraße 2, 12489 Berlin, Germany

ⁱ Max-Planck-Institut für extraterrestrische Physik, Giessenbachstrasse, 85748 Garching, Germany

ARTICLE INFO

Article history:

Received 8 June 2014

Revised 23 December 2014

Accepted 23 December 2014

Available online 9 January 2015

Keywords:

Infrared observations

Spectroscopy

Asteroids, surfaces

Comets, nucleus

Moon, surface

ABSTRACT

Spacecraft observations of atmosphereless Solar System bodies, combined with thermophysical modeling, provide important information about the thermal inertia and degree of surface roughness of these bodies. The thermophysical models rely on various methods of generating topography, the most common being the concave spherical segment. We here compare the properties of thermal emission for a number of different topographies – concave spherical segments, random Gaussians, fractals and parallel sinusoidal trenches – for various illumination and viewing geometries, degrees of surface roughness and wavelengths. We find that the thermal emission is strongly dependent on roughness type, even when the degrees of roughness are identical, for certain illumination and viewing geometries. The systematic usage of any single topography model may therefore bias determinations of thermal inertia and level of roughness. We outline strategies that may be employed during spacecraft observations to disentangle thermal inertia, level of roughness and type of topography. We also compare the numerically complex and time consuming full-scale thermophysical models with a simplified statistical approach, which is fairly easy to implement and quick to run. We conclude that the simplified statistical approach is similar to thermophysical models for cases tested here, which enables the user to analyze huge amounts of spectral data at a low numerical cost.

© 2015 Elsevier Inc. All rights reserved.

1. Introduction

The importance of roughness effects on the thermal emission properties of atmosphereless Solar System bodies was demonstrated observationally more than 80 years ago. Pettit and Nicholson (1930), and later Saari and Shorthill (1972) showed that the full Moon has a significant limb brightening, i.e., the thermal infrared radiance falls off significantly less towards the limb compared to the cosine law expected for a smooth body. Near the subsolar point, the observed radiance corresponds to an 11 μm brightness temperature just 15 K above that of a smooth body. Closer to the limb, where sunlight hits the surface at a 60° angle with respect to the local surface normal, the difference increases to 40 K, rising strongly towards the limb. Another effect,

* Corresponding author. Fax: +46 (0)18 4715999.

E-mail addresses: bjorn.davidsson@physics.uu.se (B.J.R. Davidsson), hans.rickman@physics.uu.se (H. Rickman), jbandfield@spacescience.org (J.L. Bandfield), olivier.groussin@lam.fr (O. Groussin), pedroj@iaa.es (P.J. Gutiérrez), mwilska@cbk.waw.pl (M. Wilska), mariateresa.capria@iasf-roma.inaf.it (M.T. Capria), jemery2@utk.edu (J.P. Emery), joern.helbert@dlr.de (J. Helbert), laurent.jorda@lam.fr (L. Jorda), alessandro.maturilli@dlr.de (A. Maturilli), tmueller@mpe.mpg.de (T.G. Mueller).

¹ Fax: +1 720 974 5837.

² Fax: +33 4 91 66 18 55.

³ Fax: +34 958 814 530.

⁴ Fax: +39 06 206 60188.

⁵ Fax: +1 865 974 2368.

⁶ Fax: +49 (30) 67055 303.

⁷ Fax: +49 89 30000 3272.

that was later attributed to roughness, was the unusually slow cooling of certain craters observed during lunar eclipse (Saari and Shorthill, 1963). More recent examples where resolved thermal limb brightening has been observed or modeled are found in Leyrat et al. (2011) and in Rozitis and Green (2011), respectively.

We here focus on the problem of retrieving information on sub-pixel roughness from the near and thermal infrared emission of resolved bodies, observed by spacecraft. Traditionally, analysis of resolved or disk-integrated thermal emission has been done by using thermophysical models where roughness is described by concave spherical segments, and by matching calculated spectra of infrared emission with observations (e.g., Spencer, 1990; Lagerros, 1996; Mueller, 2007). A major difficulty in such work is to disentangle roughness effects from other factors that shape the thermal emission, primarily the dependence of surface temperature on solid-state heat conduction, or more commonly, thermal inertia.⁸ However, it is not known whether the systematic usage of a particular roughness model – for example, concave spherical segments or Gaussian slope distributions – leads to biased estimates of the level of surface roughness and thermal inertia of the surface material.

The primary goal of the current work is therefore to compare four different types of rough surfaces – concave spherical segments, parallel sinusoidal trenches, random Gaussians, and fractal terrains – for cases where they all share the same degree of surface roughness, parameterized by the root mean square (RMS) slope angle s (see Section 3.1). Doing so, we also explore whether it is sufficient to describe roughness with a single parameter like s , or if there are other aspects that need to be considered as well. Concave spherical segments may be the most realistic model when studying bodies with topography dominated by cratering, such as Callisto, Mimas, and Hyperion (e.g., Prockter et al., 2010). However, resolved imaging shows that many other types of morphologies are common, and craters do not typically dominate surface roughness at small scales (Helfenstein and Shepard, 1999). Certain terrains are dominated by parallel grooves (e.g., Phobos, Thomas et al., 1979), double ridges (e.g., Europa, Triton, Prockter et al., 2010), or lineaments (e.g., Asteroid (21) Lutetia, Besse et al., 2014) – the parallel sinusoidal trench topography is perhaps a more realistic representation of such surfaces. Other landscapes are characterized by a multitude of small hills and such hummocky terrain (e.g., Odin plains on Mercury, Denevi et al., 2013) may be more realistically reproduced with random Gaussian surfaces, rather than with spherical segments. Terrains that appear rather smooth on larger scales, are sometimes revealed to have an increasingly complex topography as the resolution is improved (e.g., Asteroid (433) Eros, Cheng et al., 2002), a behavior that is perhaps best captured by fractal surfaces. We here explore whether concave spherical segments, the most common type of roughness in models, may be considered an average representative among a family of topographies, or if it is an end-member with untypical characteristics. We here do not calculate disk-integrated thermal emission spectra, but focus on resolved bodies observed by spacecraft. We consider surface terrains with a specific illumination and viewing geometry, that is characterized by a certain unresolved surface roughness.

⁸ When the heat conductivity κ , mass density ρ and specific heat capacity c_v are independent of temperature T , the solution $T(x, t)$ to the 1D heat conduction equation, with x being a dimensionless depth parameter and t is time, only depends on the thermal inertia $\Gamma = \sqrt{\kappa\rho c}$, and not on the individual values of $\{\kappa, \rho, c\}$. The thermal inertia is a measure of the degree of thermal lag, i.e., delayed adjustments of the temperature compared to changes in illumination conditions, since heating or cooling of the material occurs on finite time-scales. When $\Gamma = 0$ there is no delay, i.e., the surface temperature adjusts immediately to the prevailing illumination conditions and the material is in instantaneous thermal equilibrium with solar radiation. A non-zero thermal inertia makes the temperature and spectral radiance of a terrain functions of the previous illumination history of the terrain.

This study is timely for two reasons. Firstly, in recent years there has been a large increase in the number of spacecraft missions to Solar System bodies that carry infrared spectrometers, which means that the database of spatially resolved infrared spectral measurements has grown rapidly. Examples include Cassini to the saturnian satellites (e.g., Howett et al., 2010), Dawn to Asteroid (4) Vesta, and soon Asteroid (1) Ceres (e.g., Capria et al., 2014), Deep Impact to Comet 9P/Tempel 1, EPOXI to Comet 103P/Hartley 2 (e.g., Groussin et al., 2013), the Lunar Reconnaissance Orbiter (LRO) to the Moon (e.g., Paige et al., 2010), and Rosetta to Asteroid (2867) Šteins, Asteroid (21) Lutetia, and Comet 67P/Churyumov-Gerasimenko (e.g., Keihm et al., 2010). These spatially resolved datasets potentially offer unprecedented opportunities to extract more detailed information on the surface roughness than for unresolved targets, since Spectral Energy Distributions (SEDs) can be systematically acquired for a large variety of incidence, emergence, and azimuth angles (see Fig. 1 for definitions). If infrared emission modeling can place constraints on subpixel roughness level and type, it would certainly be an important complement to the larger-scale topography resolved by imaging datasets, as well as other location-specific context information, e.g., photometric colors, albedo, and mineralogy. Secondly, with the exception of Cassini and LRO, these spacecraft carry near-infrared spectrometers, that only sample the 3–5 μm short-wavelength tail of the SED. This wavelength range was historically not considered in analysis of disk-integrated data of unresolved objects, although a substantial increase of disk-integrated near-infrared data availability has taken place more recently, thanks to the Warm Spitzer Space Telescope observations at 3.6 μm and 4.5 μm (Trilling et al., 2010), and the WISE/NEOWISE mission observing at similar wavelengths (Masiero et al., 2014). Theoretical studies of this relatively unexplored wavelength region is particularly important, to learn how roughness level and topography type dependencies may differ, compared to those of the thermal infrared. Such knowledge is crucially important in order to define the combinations of illumination and viewing geometries that allow the thermal inertia, level of surface roughness, and type of topography to be disentangled and individually determined.

Upcoming spacecraft missions to atmosphereless bodies are even more promising in terms of thermophysical analysis. NASAs OSIRIS-REx and JAXAs Hayabusa-2 missions will return samples

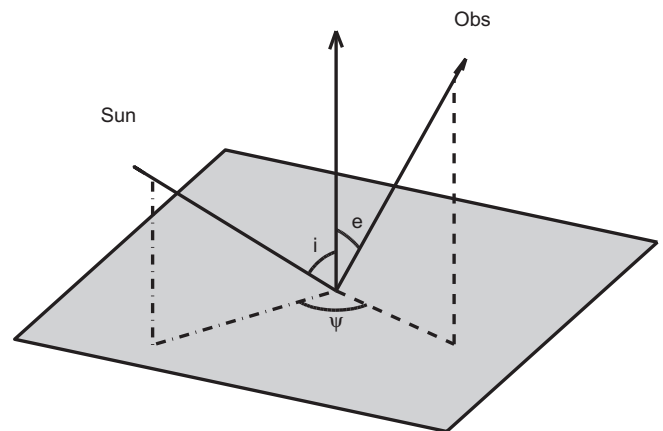


Fig. 1. Definition of angles. The incidence angle i is the angle between the outward surface normal vector and the position vector of the Sun. The incidence plane, containing the two vectors, is indicated with dashed-dotted lines. The emergence angle e is the angle between the outward surface normal vector and the position vector of the observer (Obs). The emergence plane, containing the two vectors, is indicated with dashed lines. The azimuth angle ψ is the angle measured from the incidence plane, counter-clockwise about the outward surface normal vector, towards the emergence plane.

from two different near-Earth Asteroids (101955 Bennu and 162173 1999 JU₃, respectively). The plans for these missions include global geological and spectral characterization prior to sampling in order to provide context for the returned samples and to provide a bridge between the detailed analysis of these two targets and telescopic observations. Both of these missions include thermal instruments with the goal of thermophysical characterization of the regolith. OSIRIS-REx will carry two spectrometers that together will cover the spectral range 0.4–50 μm . Current observing plans involve global mapping at seven different local times of day, including before sunrise and after sunset. The resulting data set will enable construction of a global thermal inertia map as well as investigations of anisotropies in thermal emission that may drive Yarkovsky drift and YORP torques (Lauretta, 2012). Hayabusa-2 will carry a thermal infrared imager for measuring emitted flux in a single 8–12 μm band as well as a radiometer on the MASCOT lander, both of which enable measurements of diurnal and seasonal temperature changes (Okada et al., 2014). The MarcoPolo-R mission, an asteroid sample return mission proposed to the M3 launch opportunity in ESAs Cosmic Visions program, would also have been outfitted with a dedicated thermal infrared instrument; unfortunately, MarcoPolo-R was not selected for funding.

Our secondary goal is related to the fact that spacecraft missions often generate enormous quantities of spectra that need to be analyzed. Exploring the full range of the parameter space for a large number of incidence, emergence, and azimuth angles throughout a long-duration mission, may not be feasible with full-blown thermophysical models, since they often are computationally demanding and time-consuming. For this reason, we also make a comparison between a proper thermophysical model with roughness accounted for, and a simplified statistical approach based on analytical formulas and simple numerical features that is easy to implement and computationally efficient, e.g. as part of a data reduction pipeline. Our purpose is to specify the conditions under which such an approach predicts SEDs that are quantitatively similar to those of the more sophisticated model, in order to understand when it can be applied, and when it should be avoided.

The paper is organized as follows: Section 2 is a review of processes that are responsible for roughness dependence of thermal emission from atmosphereless Solar System bodies. We also discuss various methods of accounting for roughness in modeling of thermal emission, in order to provide context for the current work. In Section 3, we discuss various parameters used to measure the level of surface roughness, describe the generation of the different terrain types, and compare their slope distributions. In Section 4 we describe the models applied here by outlining the underlying physics, and describing the parameterization, implementation, and resulting data products. Our main temperature and spectral energy distribution results are summarized in Section 5, and the comparison between advanced and simplified approaches to roughness effects in thermal emission modeling is presented in Section 6. In Section 7, examples of resolved infrared spectroscopy from Comet 9P/Tempel 1 and the Moon are presented and interpreted in the light of our modeling. Finally, Section 8 contains our discussion, recommendations and conclusions.

2. Background

The current work focuses on the atmosphereless bodies in the Solar System, in the sense that they completely lack envelopes of gas and dust, or that these are sufficiently optically thin that their effects on the thermally emitted radiation from the surface can be ignored. We thus exclude, for example, Venus, Earth, Mars and Titan from the current discussion. We include Mercury, the Moon,

asteroids, the majority of giant planet satellites, transneptunians, and comet nuclei observed from a sufficiently close distance that coma gas and dust can be ignored.

Surface roughness is one of several physical surface properties of atmosphereless bodies, that is shaped by the formation and evolution of the body, and that is accessible through remote sensing from ground, flyby or orbit. There is no formal definition of the size scale of the topography loosely referred to as “surface roughness” in the literature. Here, we take the size scale to be significantly smaller than the body curvature radius or size of global shape features, but substantially larger than the size of individual regolith grains or the typical length scale⁹ over which lateral heat conduction efficiently renders the surface locally quasi-isothermal. This translates to a lower limit in the range 0.01–0.1 m, depending on the thermal properties of the surface material, and an upper limit in the range 0.1–10 km, depending on the size of the object. The surface roughness may either be *resolved* or *unresolved*. The division line between these regimes can be anything from meters to many kilometers, depending on spacecraft instrumentation and distance from the observer to the target. Typically, the spatial resolution of infrared instruments is not as good as for optical cameras.

The degree of visually resolved surface roughness has been well documented through direct imaging during numerous spacecraft missions. In Section 3.6 we use Digital Terrain Models (DTMs) of martian satellite Phobos and Asteroid (25143) Itokawa with spatial resolutions of ~ 30 m and ~ 0.5 m, respectively, to illustrate that the degrees of surface roughness on such scales are substantially smaller than the ones required to explain the thermal emission from these bodies. Thus, the strongest effect on thermal emission apparently arise due to roughness on scales larger than 0.01–0.1 m but smaller than 1–10 m.

In the following we describe why and how roughness (unresolved by thermal instruments) affects the properties of the observed infrared emission in Section 2.1. In Section 2.2, we describe how near- and thermal-infrared observations combined with modeling can be used to determine the level of unresolved roughness.

2.1. Effect of roughness on thermal emission

A smooth blackbody surface will reach a particular physical temperature at any given moment, in accordance with the instantaneous illumination conditions, the level of thermal radiative loss to space, degree of energy transfer between the surface and interior (e.g., through solid state conduction), and if applicable, other energy sinks or sources. To an observer, the surface will emit a Planck spectrum, with a brightness temperature equal to the physical temperature. The emission is isotropic, which means that the observed radiance is independent of the emergence angle e , measured from the surface normal towards the line of sight of the observer. If the thermal conductivity is low, the observed radiance will have a simple cosine dependence on the incidence angle i , measured from the surface normal towards the Sun. There will be no dependence on the azimuth angle ψ , measured between the incidence plane (containing the surface normal and the Sun) and the emergence plane (containing the surface normal and the observer; see Fig. 1). All symbols used in the manuscript are summarized in Table 1.

A rough surface may be described as a large number of quasi-flat surface elements, all having individual tilts with respect to the average surface normal. Hence, the local incidence angle varies across the surface, giving rise to a wide range of local illumination

⁹ The thermal skin depth $l = \sqrt{\kappa \mathcal{P} / 2\pi \rho c}$ for rotation period \mathcal{P} (Spencer et al., 1989).

Table 1
Mathematical symbols and their definition.

Symbol	Description	Symbol	Description
A	Bond albedo	β	Percentile difference
\mathcal{A}	Constant	Γ	Thermal inertia
A_{gauss}	Amplitude of Gaussian	γ	Largest tilt angle of spherical segment
$a(\theta)$	Hapke slope distribution function	ε	Emissivity
B	Constant	θ	Angle between local and average normal
b	Facet surface area	$\bar{\theta}$	Hapke mean slope angle
C	constant	κ	Heat conductivity
C_t	Trench amplitude	λ	Wavelength
c	Speed of light	μ	Cotangent of i
c_v	Specific heat capacity	ρ	Mass density
D	Body diameter	ϱ	Lagerros RMS slope
\mathcal{D}	Slope distribution function	σ	Stefan–Boltzmann constant
D_f	Fractal dimension	σ_g	Parameter for generating Gaussians
e	Emergence angle	ϕ	Angle between normal and direction to other facet
F	Thermally emitted flux	ψ	Azimuth angle
\mathcal{F}	View factor	ω	RMS surface slope distribution
f	Fraction of crater coverage		
G	Phase function slope parameter		
H	Absolute magnitude		
h	Crater depth		
h_f	Fractal height scale		
h_p	Planck constant		
\mathcal{I}	Radiance emitted from terrain		
i	Incidence angle		
i, j	Indices		
J	Direct solar flux		
K	Diffuse flux		
k	Boltzmann constant		
l	Thermal skin depth		
N	Number of facets		
N_{trench}	Number of trenches		
P	Planck function		
\mathcal{P}	Rotation period		
p	Distance between facets		
p_v	Visual geometric albedo		
R	Crater curvature radius		
r	Crater rim radius		
r_h	Heliocentric distance		
S	Crater depth to curvature diameter ratio		
S_{\odot}	Solar constant		
s	RMS surface slope		
T	Temperature		
v	Visibility switch		
W	Fraction of shadowed surface		
Z	Zenith angle		
X, Y, Z	Cartesian coordinate system, illumination/viewing geometry		
x, y, z	Cartesian coordinate system, rough surface		
x_0, y_0	Position of Gaussian central axis		

conditions. If the Sun is sufficiently low in the sky, shadows will form, thus some parts of the terrain are not directly illuminated. Radiation that is scattered or emitted from one part of the surface may intercept another part of the surface and get absorbed – a phenomenon known as self illumination or self heating. Therefore, shadowed regions may be illuminated to a certain degree by diffuse radiation. The combination of surface element tilts, shadows and self heating makes the physical temperature vary drastically across the surface at any given moment, at length scales large enough to render lateral heat conduction inefficient. To an observer, the SED of the unresolved rough terrain may not be well described by a Planck function, since it is a superposition of several such functions, evaluated for a wide range of temperatures. Or, in other words, the sum of several Planck functions is not a Planck function. It is meaningless to interpret the brightness temperature in terms of a single physical temperature since the real temperature dispersion of the surface is significant. The observed radiance is no longer isotropic but depends strongly on the incidence, emergence and azimuth angles. If the observer has the Sun in the back, and predominantly sees strongly sunlit parts of the surface, the

observed radiance may be considerably higher than that of a smooth surface – a phenomenon known as *beaming* (e.g., Hansen, 1977, see also Fig. 9 in Rozitis and Green, 2011). However, if the Sun is low in the sky and illuminated surface elements are hidden from the observer behind topography, the large domination of shadows in the field of view will result in an observed radiance substantially lower than that of a smooth terrain under similar illumination and viewing conditions. For these reasons, surface roughness has a strong effect on the emitted near-infrared and thermal radiation.

2.2. Modeling the thermal emission of rough surfaces

To illustrate the importance of accounting for roughness in modeling of thermal emission, the squares in Fig. 2 show the 10.6 μm magnitude of Asteroid (1) Ceres as function of phase angle (the angle between the Sun and the observer as seen from the target, counted negative pre-opposition), according to Spencer (1990). Note that the data has been normalized to a heliocentric distance of 3 AU for Ceres, and an observer-asteroid distance of 1 AU. The

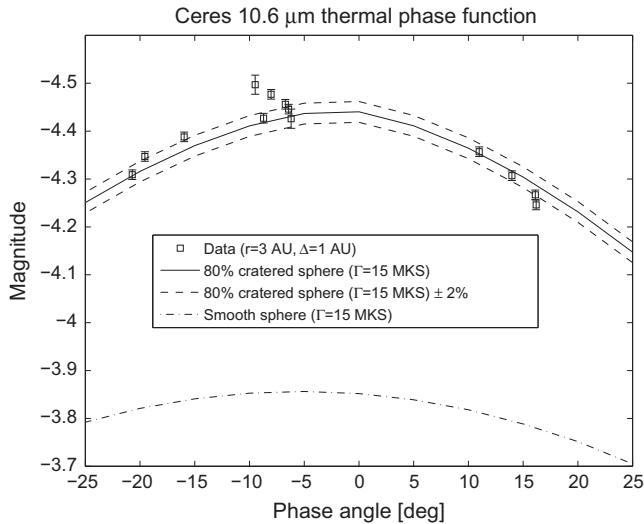


Fig. 2. Observed 10.6 μm magnitude of Asteroid (1) Ceres as function of phase angle (negative pre-opposition) versus models. The magnitudes are reduced to a heliocentric distance of 3 AU and an observer-object distance of 1 AU. The dashed-dotted curve corresponds to a smooth sphere, while the solid curve corresponds to a spherical body with 80% of its surface covered by hemispherical craters ($s = 44^\circ$). In both cases, the diameter is $D = 933$ km and the thermal inertia is $\Gamma = 15$ MKS. Dashed curves show the rough case solution with $\pm 2\%$ variation in terms of flux.

data is compared to the dashed-dotted curve, showing the corresponding phase function expected for a smooth sphere of diameter $D = 933$ km, the occultation diameter of Ceres as used by Spencer (1990). The model was run for a thermal inertia of $\Gamma = 15 \text{ J m}^{-2} \text{ K}^{-1} \text{ s}^{-1/2} = 15$ MKS, appropriate for Ceres (Spencer, 1990). The modeled disk-integrated spectral radiance of the smooth sphere is a factor ~ 1.7 lower than the observed radiance, which is significant compared to the uncertainty of the measurements.

In order to explain the lunar observations of Pettit and Nicholson (1930) and Saari and Shorthill (1963), a thermophysical model was developed by Buhl et al. (1968a,b), that explicitly treated the shadowing and self heating taking place on a body with a rough surface. This was done by considering a fraction f of the surface covered by “craters” shaped as concave spherical segments, while a fraction $1 - f$ remained smooth. Temperatures were calculated for each point within the crater, and for the smooth surface, for a variety of illumination conditions. Radiances could then be calculated for both resolved and unresolved craters, at any given point on the lunar surface. Similar approaches were used by Hansen (1977) and Spencer (1990) to model the thermal infrared phase functions of Main Belt Asteroids. Disk-integrated radiances were obtained by carefully considering the actual incidence, emergence and azimuth angles for all parts of the body visible to the observer, and summing their contributions. For example, Spencer (1990) demonstrated that a $f = 0.8$ coverage of hemispherical craters could explain the phase function of Ceres (corresponds to RMS mean slope $s = 44^\circ$, see Eq. (1)), using the occultation diameter $D = 933$ km and applying $\Gamma = 15$ MKS. We use the model by Davidsson and Rickman (2014) to reproduce and confirm this result, as shown by the solid curve in Fig. 2. When roughness is introduced the beaming elevates the model radiance to the observed level. The asymmetry is due to thermal inertia on a prograde rotator – the warmer evening terminator is visible pre-opposition, resulting in a higher radiance (more negative magnitude), and the cooler morning terminator comes into view post-opposition. Due to the success of this kind of model to explain lunar and asteroid observations, and due to the mathematical

simplicity following from the geometric symmetry, the concave spherical segment formalism has become the standard approach when modeling roughness effects (see, e.g., Giese and Kürt, 1990; Kürt et al., 1992; Lagerros, 1996; Lagerros, 1997; Emery et al., 1998; Müller and Blommaert, 2004; Harris et al., 2005; Delbò et al., 2007; Mueller, 2007; Delbò and Tanga, 2009; Rozitis and Green, 2011; Stansberry et al., 2012).

In the asteroid scientific community, models like these are referred to as Thermo-Physical Models, or TPMs. A TPM allows the user to accurately determine the physical size, visual geometric albedo, bolometric Bond albedo, level of surface roughness, and thermal inertia of atmosphereless Solar System bodies. However, this is normally only possible if the target has been observed at multiple wavelengths for a wide range of pre- and post-opposition phase angles, if the body shape, spin period and spin pole orientation are known from lightcurve inversion or spacecraft flyby, and if the absolute magnitude H and slope parameter G are known (the HG-magnitude system is described by Bowell et al. (1989)). Among the thousands of objects observed in the thermal infrared portion of the spectrum from ground, or by spaceborne observatories like *IRAS*, *ISO*, *Spitzer*, *Herschel*, *WISE*, and others, only a handful are sufficiently well characterized to motivate the application of a TPM.

It is therefore clear that TPMs are extremely important tools in Solar System science, despite some practical limitations due to data availability. For nearly half a century, the majority of these TPMs have relied on the concave spherical segment to describe roughness. In the following, we use TPMs to explore the similarities and differences between spherical segments and other possible types of surface topography. However, first we need to recapitulate various ways to measure the degree of roughness, and describe the different forms of topography considered in this paper.

3. Different types of roughness

We define here two different parameters used to measure the level of roughness – the root mean square (RMS) slope angle s , and the Hapke mean slope angle $\bar{\theta}$. We also describe in some detail how the concave spherical segments, parallel sinusoidal trenches, random Gaussians, and fractal surfaces are generated. Finally, we show examples of the slope distributions for the different surfaces.

3.1. Measures of the level of roughness

In many practical applications, there is a need to express the level of roughness of a terrain with a single parameter. There are many ways of doing this, and the usage of a specific parameter varies between different scientific communities, for historical reasons. In the context of thermal emission from atmosphereless Solar System body surfaces, the RMS surface slope s is common. Following Spencer (1990), it is defined as

$$s = \sqrt{\frac{\sum_{i=1}^N \theta_i^2 b_i \cos \theta_i}{\sum_{i=1}^N b_i \cos \theta_i}}. \quad (1)$$

It is here assumed that the rough terrain can be broken up into N locally flat facets, where facet i has surface area b_i and a surface normal that is making an angle θ_i with respect to the average surface normal of the terrain. In essence, s^2 is the average value of θ^2 in radians, weighted by the projection of the surface area along the local vertical.

One reason for the popularity of the RMS slope angle is that the thermal emission from concave spherical segments (including flat surroundings) remains the same for different combinations of crater surface coverage f and the ratio between crater depth and curvature diameter S , as long as s is constant. According to Lagerros (1996), s , f , and S are related as,

$$s = \sqrt{\frac{f}{2} \left(\gamma^2 - \frac{(\gamma \cos \gamma - \sin \gamma)^2}{\sin^2 \gamma} \right)}, \quad (2)$$

where $\cos \gamma = 1 - 2S$, and γ is the largest slope angle of the spherical segment. Thus, for any given s -value, there is a family of corresponding $\{f, S\}$ values. To an observer with a thermal infrared instrument, unresolved terrains with few but deep craters will be indistinguishable from a terrain with many shallow craters, if their s -values are identical. Spencer (1990) illustrated this numerically for two disk-integrated spheres having surface roughness characterized by $\{f, S\} = \{0.500, 0.413\}$ and $\{f, S\} = \{1.000, 0.179\}$, respectively, both having $s = 33.7^\circ$. In spite of the difference in topography, the thermal emission properties of the bodies were identical. Spencer (1990) therefore speculated that other types of topographies would also display similar thermal emission properties, for similar values of s . In order to test this hypothesis, we use the RMS mean slope value s as the common parameter for the generation of spherical segments, sinusoidal trenches, random Gaussians and fractal terrains. In particular, we focus on three levels of roughness, $s = 5^\circ, 20^\circ$, and 35° . For comparison, the terrain used in Fig. 2 to reproduce the phase curve of Ceres has $s = 44^\circ$.

Among the several other parameters used to measure the level of roughness, we also choose to describe the Hapke mean slope angle $\bar{\theta}$, which has gained widespread popularity in the context of retrieving the level of roughness of Solar System bodies from observations of their visual phase functions. The parameter $\bar{\theta}$ is defined by Hapke (1984, 1993). The basic assumption is that the distribution of slopes angles $a(\theta)$ of a terrain is given by a Gaussian function,

$$a(\theta) = \mathcal{A} \exp\left(-\frac{\tan^2 \theta}{B}\right) \frac{\sin \theta}{\cos^2 \theta}. \quad (3)$$

The shape of the distribution is regulated by the parameters \mathcal{A} and B . If they are known for a particular terrain, one can then calculate the Hapke mean slope angle as

$$\tan \bar{\theta} = \frac{2}{\pi} \int_0^{\pi/2} a(\theta) \tan \theta d\theta. \quad (4)$$

Another assumption built-into this model is that the slopes on a surface predominantly are small. This allow us to specify approximate expressions for \mathcal{A} and B in terms of $\bar{\theta}$,

$$\begin{aligned} \mathcal{A} &\approx \frac{2}{\pi \tan^2 \bar{\theta}} \\ B &\approx \pi \tan^2 \bar{\theta}. \end{aligned} \quad (5)$$

In other words, if $\bar{\theta}$ is known, it completely determines both \mathcal{A} and B , thus $a(\theta)$ itself. Alternatively, if the slope angle distribution can be determined for a terrain by direct measurements, and if the distribution turns out to have a Gaussian shape, one may use the fitted \mathcal{A} or B values to calculate the Hapke mean slope angle $\bar{\theta}$ of the surface. The gradual break-down of consistency between Eqs. (3)–(5) with growing $\bar{\theta}$ was discussed by Davidsson et al. (2009).

We now proceed in Sections 3.2–3.5 to provide the mathematical definitions of the topographies used in this work. Their resulting slope angle distributions, in comparison with each other and those of observed targets, are discussed in detail in Section 3.6.

3.2. Concave spherical segments

A $1 \times 1 \text{ m}^2$ area in a x - y -plane is broken up into a quadratic grid with 1024 squares. For each node on the grid, a z -value is assigned, that is zero outside a circular rim centered on $x = y = 0$ with radius $r = 0.437 \text{ m}$, in order to produce a crater coverage of $f = 0.6$. Within the rim, the z -coordinate is given by

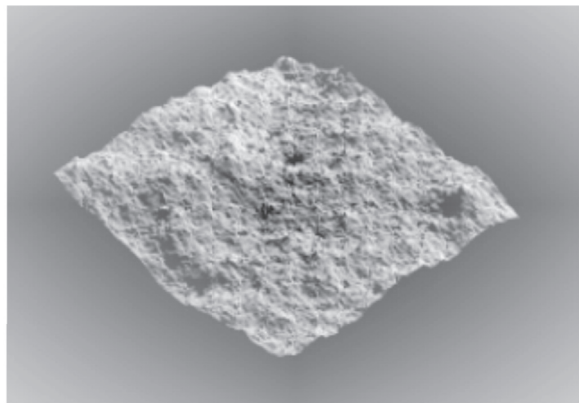
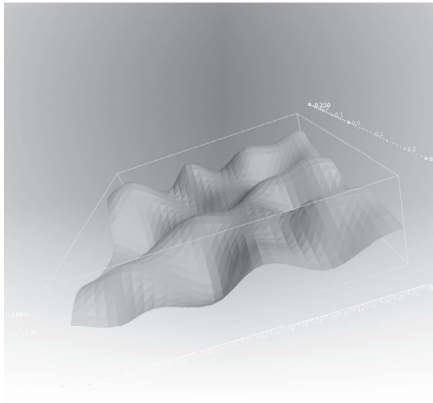
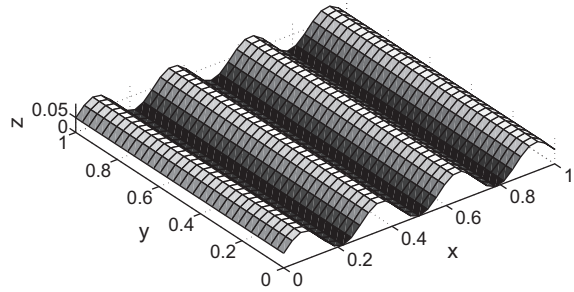
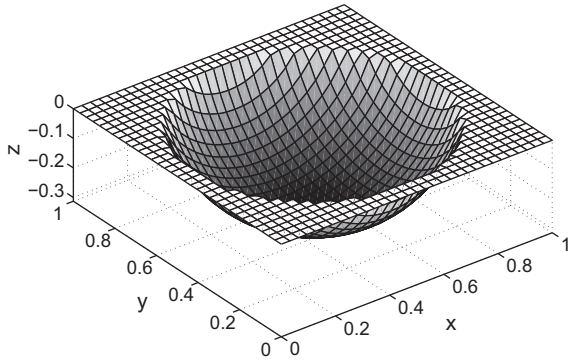


Fig. 3. Graphical representations of the four roughness types (all having $s = 35^\circ$). Upper left: concave spherical segment. Upper right: parallel sinusoidal trenches. Lower left: random Gaussians. Lower right: fractals. Note that 2048 surface facets are used for the first three terrains, while the fractal surface is built by using about 33,000 facets.

$$z = R - h - \sqrt{R^2 - x^2 - y^2}, \quad (6)$$

thus giving the terrain within the rim the shape of a concave spherical segment. Here, h is the crater depth and $R = (r^2 + h^2)/(2h)$ is the curvature radius of the spherical segment. By varying h , different degrees of roughness are obtained. The four nodes on the terrain surface corresponding to a particular square in the x - y -plane are used to form two triangular facets. The total number of triangular facets on the surface is thus 2048. For each facet the surface area is calculated, as well as the normal vector and its tilt with respect to the z -axis. These are used to calculate the RMS slope angle s according to Eq. (1). We produce spherical segment terrains with $s = 5^\circ, 20^\circ$, and 35° by using $h = 0.0359$ m, 0.151 m, and 0.313 m, respectively. If the corresponding $\{f, S = h/2R\}$ values are used to calculate s according to Eq. (2), they differ slightly from the actual s -values of the terrains, since the finite resolution of the numerical representation of craters prevents them from being a mathematically perfect spherical segment. A graphical representation of the $s = 35^\circ$ spherical segment is seen in the upper left panel of Fig. 3.

We emphasize that the arbitrary selection of $f = 0.6$ when generating spherical segments with a particular s does not restrict the validity of our simulations. For example, we verified that the nominal $\{f, S\} = \{0.6, 0.106\}$ model is similar to a $\{f, S\} = \{0.41, 0.156\}$ model, both having $s = 20^\circ$. This was tested for a number of $\{i, e, \psi\}$ combinations, showing that the $3 \leq \lambda \leq 20$ μm radiances were identical to within $\leq 1\%$, except for very high incidence angles ($i = 80^\circ$) where resolution limitations led to $\sim 15\%$ differences at short wavelengths ($\lambda \approx 5$ μm). Thus, the similarity of different $\{f, S\}$ combinations with the same s for spherical bodies discussed in Section 3.1 is not merely valid for disk-integrated SEDs, but also for individual $\{i, e, \psi\}$ combinations for single unresolved craters with flat surroundings.

3.3. Parallel sinusoidal trenches

In order to create a set of parallel sinusoidal trenches, we apply the same quadratic grid in the x - y -plane as used in Section 3.2. However, here the z -coordinates for each node is given by

$$z = C_t + C_t \sin(2\pi(N_{\text{trench}} + 0.5)x) \quad (7)$$

that gives rise to $N_{\text{trench}} = 3$ trenches, running parallel to the y -axis. The level of roughness is regulated by the amplitude C_t . Based on the Cartesian node positions, 2048 triangular surface facets are constructed, and s is calculated as for spherical segments. In order to achieve $s = 5^\circ, 20^\circ$, and 35° , we apply $C_t = 0.00575$ m, 0.02438 m, and 0.04912 m (upper right panel of Fig. 3). In these simulations, which consider equatorial regions on a body with the spin pole perpendicular to its orbital plane, trenches are assumed to run parallel to the north-south meridian. We emphasize that our results are valid for this particular orientation – for example, if the trenches run parallel to the equator, the SEDs are different. This orientation was selected to illustrate the behavior of trenches when shadowing appears at high incidence angles, as for the other terrains.

3.4. Random Gaussians

In order to generate a rough surface with random Gaussians, as previously, the same grid in the x - y -plane as described in Section 3.2 is used. The z -coordinate for each node is then defined as a superposition of different Gaussian functions randomly generated both in amplitude, width and location. From a practical point of view, a smooth plane is considered as a starting surface. Then, random Gaussian functions are generated and successively added to

the modified surface until the desired RMS mean slope s is reached. Each added Gaussian modifies the z -coordinate of the $[x, y]$ node as

$$z(x, y) = z_0(x, y) + \frac{A_{\text{gauss}}}{2\pi\sigma_g^2} \exp\left(-\frac{(y - y_0)^2 + (x - x_0)^2}{2\sigma_g^2}\right), \quad (8)$$

where $z_0(x, y)$ is the z -coordinate before adding the new generated Gaussian, and other quantities are defined as,

$$\begin{cases} A_{\text{gauss}} = C \cdot \text{rn}[-1, 1] \\ \sigma_g = 2.25 + 0.75 \cdot \text{rn}[0, 1] \\ x_0 = 16 \cdot \text{rn}[-1, 1] \\ y_0 = 16 \cdot \text{rn}[-1, 1] \end{cases} \quad (9)$$

in which $\text{rn}[-1, 1]$ and $\text{rn}[0, 1]$ are uniformly generated real random numbers within the intervals $[-1, 1]$ and $[0, 1]$, respectively. C is a constant which depends on the desired roughness level. In the present simulations $C = 0.25, 0.45$, and 0.65 are used in order to produce surfaces with $s = 5^\circ, 20^\circ$, and 35° , respectively. The values that σ_g may take, lead to a FWHM of the Gaussians between 0.16 – 0.22 m, or 5 – 7 times the distance between nodes in the x - y -plane. Finally, in the previous expressions for x_0 and y_0 , standing for the center of the Gaussian function, the factor 16 is coming from the fact that the initial surface is divided in 1024 squares. It is possible to define other Gaussian functions (i.e., different amplitude and width) leading to rough surfaces with a different character (e.g. more spiky than those used in this study) but all sharing the same RMS slope s . After several tests, the constants characterizing the amplitude and width in the aforementioned expressions were selected because they allow achieving the desired RMS with a comparatively small number of added Gaussian functions, usually less than 200. An example of a random Gaussian surface is shown in the lower left panel of Fig. 3.

Given the random nature of the Gaussian surfaces, it is logical to expect that different surfaces with the same s (what we could call different *realizations* of the same roughness level) lead to different emission spectra depending on the incidence and emergence angles. First, several tests were performed by using three different realizations each for $s = 5^\circ, 20^\circ$ and 35° . From these calculations, we found that the maximum dispersion in the spectra ranged (with regard to the average value) from 2% (for small incidence/emergence angles) up to 8% (for large incidence/emergence angles). Given these values for the dispersion, if the spectra estimated from different realizations of the same surface are considered as measurement errors, according to error theory the spectra obtained from the average of six different realizations could be considered, in principle, as representative. Accordingly, simulations have been performed for six different random Gaussian surfaces for the three s -values of this study. When the spectra of the six different realizations are analyzed the maximum dispersion (with regard to the average value) increases up to 15% for large incidence/emergence angles. This implies that the number of surface realizations is still poor for a significant statistical representation at large incidence/emergence angles. Because the main goal was to provide an example of the behavior of the spectra, six different realizations of Gaussian surfaces with the same s -value was considered as a reasonable compromise.

3.5. Fractals

We generate the fractal terrain using the “midpoint FM2D” algorithm (Saupe, 1991; Barnsley et al., 1988), that uses a midpoint random displacement method to produce fractal landscapes. The random numbers follow a Gaussian distribution, thus the resulting slope distribution is similar to that of the Gaussian terrain. An example of a terrain created by this algorithm is displayed in the

lower right panel of Fig. 3, with 32,768 facets. The fractal terrain has two parameters, the fractal dimension D_f and the height scale h_f . The fractal dimension D_f defines the scale to which the self-affine nature of the terrain applies, and varies between 2.0 (smooth) and 3.0 (very rough) for a surface. A large fractal dimension means more variations at small scale. The height scale h_f is the standard deviation of height at a given scale, and increases with increasing roughness. Planetary surfaces have a typical fractal dimension D_f in the range 2.1–2.5 and a height scale h_f of 0.02–0.46 m (e.g., Cheng et al., 2002). Two surfaces with comparable fractal dimension but different height scale have a different degree of roughness. The parameters D_f and h_f are coupled, since both increase with increasing roughness. In this work, we choose to fix the fractal dimension D_f to a typical value of 2.2, and to vary h_f in order to retrieve a RMS slope s of 0° ($h_f = 0$ cm), 5° ($h_f = 0.8$ cm), 20° ($h_f = 3.7$ cm) and 35° ($h_f = 7.7$ cm, lower right panel of Fig. 3).

3.6. Distributions of slope angles

We here calculate the slope angle distributions $\mathcal{D}(\theta)$ numerically for the various terrains. Fig. 4 shows $\mathcal{D}(\theta)$ for the sinusoidal trench, spherical segment, and random Gaussian terrains, as asterisks, while the $\mathcal{D}(\theta)$ of fractals is shown as rings. Even though the terrains have $s = 35^\circ$ in all cases, the slope distributions are significantly different with respect to each other. The sinusoidal trench distribution has a pronounced peak at $\theta \approx 35^\circ$ – 50° , due to the large coverage of steep trench walls. The rather narrow peak in the slope distribution shows that the parallel trench surface has a high degree of systematics, in the sense that certain slopes are occurring repeatedly on the terrain. However, ridge peaks and trench floors provide a low-level background of small- θ slopes, lowering the average to $s = 35^\circ$. Among the terrains considered here, the trenched surface has the smallest maximum slope angle; only 55° .

The spherical segment is unique in having a strong isolated peak at $\theta = 0^\circ$, since 40% of the projected terrain area here is flat. The crater itself provides a range of slopes, reaching just over 70° , which is the most extreme tilt found on any terrain considered

here. This distribution is less peaked than that of the parallel trenches, since the degree of normal vector repetition is lower.

The random Gaussian and fractal surfaces are similar to each other and have the smoothest and most gradually changing slope distribution of the terrains investigated here. They have the highest degree of randomness for normal vector orientations, resulting in a broad slope distributions.

The slope distributions of these numerically generated terrains do not necessarily resemble Gaussian distributions, hence we use the symbol $\mathcal{D}(\theta)$ to distinguish them from proper Gaussian slope distributions $a(\theta)$. Nevertheless, we now use Eq. (4), with $\mathcal{D}(\theta)$ replacing $a(\theta)$, to calculate corresponding $\bar{\theta}$ -values for the terrains. Such numerically evaluated $\bar{\theta}$ -values are then inserted into Eqs. (3) and (5) to obtain the corresponding Gaussian $a(\theta)$. A distribution $a(\theta)$ obtained in this manner, may be considered the closest possible match the formalism of Hapke (1984) has to offer, to the actual slope angle distribution. By comparing $\mathcal{D}(\theta)$ and $a(\theta)$ distributions in this manner, we also illustrate the suitability of the Hapke formalism for the particular topographies studied here.

For the surfaces considered here we obtain $24.5^\circ \leq \bar{\theta} \leq 28.4^\circ$, where the rather small spread is consistent with the fact that s is constant. The corresponding Gaussian distributions according to Eqs. (3) and (5) are shown as solid curves in Fig. 4. Clearly, sinusoidal trenches and spherical segments are poorly described by the distribution used by Hapke (1984). Particularly, the sinusoidal trench terrain $\mathcal{D}(\theta)$ peaks at large θ , while the $a(\theta)$ -distribution is substantially broader. Except for the singularity at $\theta = 0^\circ$, the spherical segment $\mathcal{D}(\theta)$ is qualitatively similar to $a(\theta)$, although the two distributions do not peak at the same slope angle. However, the random Gaussian and fractal terrains are well represented by $a(\theta)$, particularly at small slopes, although the fit is not perfect around the peak.

We have compared these synthetic distributions to actual slope distributions for a few bodies for which there exist DTMs. For example, the $3.15 \cdot 10^6$ facet shape model of the martian satellite Phobos (Gaskell, 2011) was divided into $10^\circ \times 10^\circ$ longitude and latitude patches, each lacking significant global curvature and on average containing ~ 4800 facets, with a mean equivalent diameter of 27 m. For 95% of the patches, the local $\bar{\theta}$ ranged between $0.5^\circ \leq \bar{\theta} \leq 9.9^\circ$ with an average of $\langle \bar{\theta} \rangle = 5.2^\circ$, that corresponds to a RMS slope angle $s = 9.0^\circ$. If $\gamma = 75^\circ$ concave spherical segments are used to describe roughness, this corresponds to a crater coverage of $f = 3.8\%$. This can be compared to the value $f = 90\%$ determined by Kürt et al. (1992) when matching the calculated thermal emission of $\gamma = 75^\circ$ craters at 4.7–6.6 μm and 14.3–15.9 μm to the observed fluxes acquired by the Soviet spacecraft Phobos-2. The measured degree of roughness corresponds to $s = 44^\circ$. Therefore, surface irregularity on the size scale of several tens of meters contributes to the roughness on Phobos ($s = 9^\circ$), but a stronger contribution occurs due to smaller features.

We did a similar analysis for Asteroid (25143) Itokawa, with a shape model consisting of $3.15 \cdot 10^6$ facets (Gaskell et al., 2008), divided into $5^\circ \times 5^\circ$ longitude and latitude patches, each containing an average of ~ 1100 facets with a mean equivalent diameter of 0.4 m (a factor ~ 70 better resolution than for Phobos). For 95% of the patches, the local $\bar{\theta}$ ranged between $0.4^\circ \leq \bar{\theta} \leq 12.3^\circ$ with an average of $\langle \bar{\theta} \rangle = 5.5^\circ$, that corresponds to a RMS slope angle $s = 9.4^\circ$, values that are similar to those of Phobos. Groundbased N- and Q-band observations of Asteroid (25143) Itokawa were analyzed by Müller et al. (2005), by using a thermophysical model with roughness modeled as concave spherical segments. The level of roughness could not easily be determined, but a crater coverage of $f < 10\%$ for a crater RMS slope of $q < 0.3$ (as defined by Lagerros, 1998), corresponding to $\gamma = 53^\circ$ and $s < 19^\circ$, was considered unlikely. By contrast, their default combination $f = 60\%$ and $q = 0.7$ used for large mainbelt asteroids, corresponding to

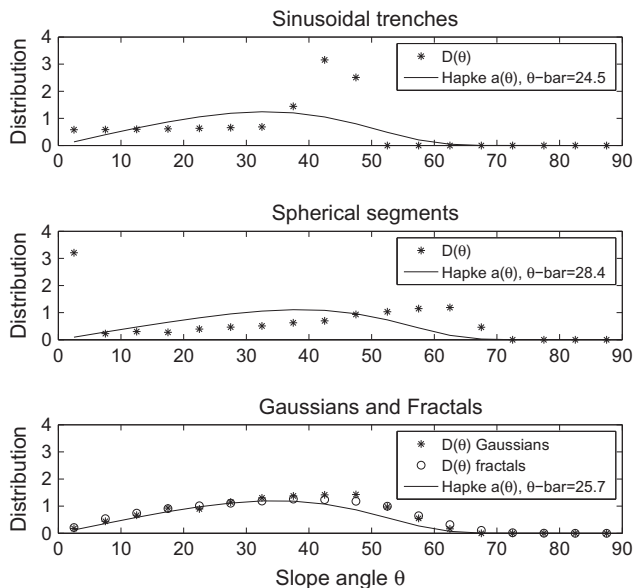


Fig. 4. Numerical slope angle distributions $\mathcal{D}(\theta)$ as asterisks or rings, compared to Hapke distributions $a(\theta)$ as solid curves for sinusoidal trenches, spherical segments, random Gaussians and fractal surfaces with $s = 35^\circ$.

$s = 35^\circ$, was consistent with the observations. Thus, an increase in roughness on centimeter scale is required.

The slope distributions are often well matched by the Hapke formalism (Eqs. (3) and (5)), both for Phobos and Itokawa. In these cases, synthetic surfaces generated by random Gaussian functions or fractals are particularly suitable. However, there are terrains with prominent blocks on Itokawa, and fields with large craters on Phobos, that are not well represented by Hapke-style slope distributions. Smooth fields on Phobos that contain angular blocks have distributions with prominent high- θ tails not captured by Eqs. (3) and (5). Single well-resolved craters with surrounding quasi-smooth terrains on Phobos, similar in appearance to the upper left panel of Fig. 3, are not necessarily well represented by slope distributions generated for concave spherical segments, such as in the middle panel of Fig. 4. However, if flat terrain is replaced by a large number of shallow craters, in addition to a single deep crater, synthetic distributions are qualitatively similar to observed ones. We emphasize that DTM slope distributions may be misleading in the context of thermophysics, as they may change in character when extending to roughness on scales below the resolution of the image used to retrieve them. Roughness on such sub-resolution size scales appears to dominate the properties of thermal emission, as long as the features are larger than the thermal skin depth.

4. Modeling

We calculate the radiance at different wavelengths (1–100 μm SEDs) that would be measured by an infrared instrument observing these model terrains under specific illumination and viewing conditions. This wavelength range includes the Planck peaks at temperatures in the range $30 \leq T \leq 400$ K encountered locally on bodies at 1 AU from the Sun. We consider the global body shape to be well resolved, and consider small unresolved patches of surface in distinct locations, that have different subpixel topographies. We focus on characterizing differences and similarities between the classical spherical segments, and the other three topographies, also using SEDs of smooth surfaces for reference. In order to explain the differences among the SEDs, we also present subpixel surface temperature distributions. In order to isolate roughness dependencies, we here only consider cases with zero thermal inertia. We consider cases with a complete treatment of surface facet tilts, cast shadows, self heating, facet–facet and facet–observer visibilities, but also consider cases where self heating is ignored, to understand the relative importance of shadowing, tilts and self heating for the resulting SEDs. Based on these simulations, we formulate observational strategies that can be applied to simplify the problem of breaking degeneracies and to estimate thermal inertia, level of roughness, and the type of surface roughness more reliably.

4.1. Modeling the surface temperature of a terrain

A thermophysical model calculates surface temperatures by balancing a number of energy sources and sinks. The energy sources considered here are direct solar illumination, and infrared self heating. For simplicity, the current simulations assume zero albedo at all wavelengths, which means that no scattering takes place. The only energy sink consists of thermal emission. There is no conductive heat sink or source since we assume $\Gamma = 0$, hence no thermal lag. These simplifications are intentional, in order to isolate effects due to differences in topography. Most computer codes used for these calculations do have the capacity to consider non-zero thermal inertia, as well as non-zero albedo, with multiple-scattering accounted for.

The flux of incident direct solar radiation for a given illuminated facet i is given by

$$J_i = \frac{S_\odot v_i \cos \mathcal{Z}_i}{r_h^2} \quad (10)$$

Here, $S_\odot = 1360 \text{ J m}^{-2} \text{ s}^{-1}$ is the solar constant, \mathcal{Z}_i is the local zenith angle (angle between the local surface normal and the direction towards the Sun), r_h the heliocentric distance, and v_i is a visibility switch, taking the value unity if the facet is illuminated and zero if it is in shadow. Thus, the only practical difficulty in evaluating J_i for a given surface is to determine v_i , which is done by ray casting.

If the element has surface temperature T_i , it will emit a radiative flux according to

$$F_i = \sigma T_i^4, \quad (11)$$

where σ is the Stefan–Boltzmann constant. Since a zero albedo is assumed at all wavelengths, Kirchhoff's law requires that the integrated hemispherical emissivity (ratio between thermally emitted spectral radiance of a surface, integrated over wavelength and all directions, compared to that of a blackbody, see, e.g., Hapke, 1993) is unity.

The diffuse radiation field constituting the infrared self heating is given by

$$K_i = \sigma \sum_{j \neq i}^N \mathcal{F}_{ij} T_j^4. \quad (12)$$

Here, the view factors \mathcal{F}_{ij} determine what fraction of the flux produced by facet j that illuminates facet i . For definitions and detailed discussions of the view factor, see e.g., Özişik (1985), Lagerros (1997), Davidsson and Rickman (2014). View factors are calculated as

$$\mathcal{F}_{ij} = \frac{v_{ij} b_j \cos \phi_i \cos \phi_j}{\pi p_{ij}^2} \quad (13)$$

where b_j is the area of facet j , p_{ij} is the distance between the centers of facets i and j , ϕ_i is the angle between the outward surface normal of i and the vector pointing towards j , while ϕ_j is the angle between the outward surface normal of j and the vector pointing towards i . This formalism assumes that radiation is emitted isotropically from each facet. The visibility factor v_{ij} equals unity if the path between facets i and j is free from intervening topography, and if the facets are facing each other ($\phi_i > 0$ and $\phi_j > 0$) – otherwise, $v_{ij} = 0$. As before, visibility is determined through ray casting.

The energy balance of the surface requires that $J_i + K_i = F_i$, i.e., the equation to be solved is

$$\frac{S_\odot \cos \mathcal{Z}_i v_i}{r_h} + \sigma \sum_{j \neq i}^N T_j^4 \frac{v_{ij} b_j \cos \phi_i \cos \phi_j}{\pi p_{ij}^2} = \sigma T_i^4. \quad (14)$$

A simple way of solving this equation is to step forward with small time increments, let \mathcal{Z}_i evolve according to body rotation, calculate self heating based on temperatures T_j valid for the previous time step, and readily evaluate T_i at the current time step for all facets i .

The energy balance described by Eq. (14) can be modified by a number of processes, such as energy transport e.g., by heat conduction, energy consumption e.g. due to sublimation of ice, or energy release by, e.g., crystallization of amorphous ice. Such processes are not considered here since our main goal is to study the effect on SEDs when varying the surface morphology while keeping the degree of roughness constant.

4.2. Modeling the spectral energy distribution of a terrain

There are essentially two data products for each combination of topography, degree of surface roughness, and $\{i, e, \psi\}$ combination – the temperature of each facet (used to build histograms), and

Spectral Energy Distributions (SEDs). In order to build a SED, the Planck functions of each facet are first calculated,

$$P_i(\lambda) = \frac{2h_p c^2}{\lambda^5} \left(\exp\left(\frac{h_p c}{k \lambda T_i}\right) - 1 \right)^{-1} \quad (15)$$

in SI units, which is multiplied by 10^{-6} to yield the unit $[\text{W m}^{-2} \text{sr}^{-1} \mu\text{m}^{-1}]$, i.e., we express the spectral radiance per micrometer. The Planck constant, speed of light, and Boltzmann constant are denoted by h_p , c , and k , respectively. The SED measured by a detector unable to resolve the terrain is given by

$$\mathcal{I}(\lambda) = \frac{\sum_{i=1}^N P_i b_i v_i \cos e_i}{\sum_{i=1}^N b_i v_i \cos e_i} \quad (16)$$

i.e., the SED is the average P_i , weighted by the projected surface area. Note that $v_i = 1$ for facets visible to the detector, but $v_i = 0$ otherwise. Thus, ray casting is needed also to calculate the SEDs. Although we generally calculate 1–100 μm SEDs, we typically focus on wavelengths below 20 μm , in order to avoid potential problems with decreasing opacity (hence, contributions from sub-surface emission) at far-infrared wavelengths.

4.3. Thermophysical codes

Eqs. (10)–(14) are used to calculate the temperature for each facet of the terrain, depending on its incidence angle. Projected shadows are taken into account for all kinds of rough terrains, and self heating is accounted for in all cases except fractal terrains. The temperature of each facet and the total spectral energy distribution of the terrain are calculated, while taking visibility of each facet into account. For practical reasons, these calculations are made using a number of different numerical computer codes:

- Concave spherical segments: the numerical code was written in MATLAB and FORTRAN by Davidsson and Rickman (2014) and takes into account projected shadows and self heating.
- Parallel sinusoidal trenches: the numerical code is identical to the concave spherical segments code.
- Random Gaussian surface: the numerical code was written in FORTRAN by Gutiérrez et al. (2001) and takes into account projected shadows and self heating.
- Fractal surface: the numerical code was written in C language by Groussin et al. (2013) and takes into account projected shadows but not self heating.

These different numerical codes differ slightly in their implementation, but we confirmed that they resulted in the same temperature and spectral energy distribution in the case of a flat surface with $i = e = 0$.

4.4. A simplified statistical model

The simple statistical model shown here is similar to that described by Bandfield and Edwards (2008) and Bandfield (2009). This is a computationally efficient approach that models any given surface in ~ 1 s of computer time, allowing for the comparison of model results with large numbers of observations that are becoming more common with spacecraft datasets. In this model, surface temperatures are predicted for slopes of zero to 90° (at 2° intervals) and azimuth orientations of zero to 360° (at 20° intervals). Modeled temperatures assume radiative equilibrium and sloped surfaces include a self heating component proportional to the fraction of their hemispherical field of view filled by adjacent surfaces rather than space. The self heating radiance is calculated assuming it is coming from a horizontal surface at radiative

equilibrium. The assumption of radiative equilibrium is only appropriate for daytime surfaces of slowly rotating bodies with low thermal inertia, such as Earth's Moon. Under these conditions, surface temperatures predicted using heat diffusion models are within ~ 1 K of radiative equilibrium. This methodology is inappropriate for nighttime measurements, or when thermal inertia and rotational period lead to significant deviations from radiative equilibrium conditions. In such cases, it is possible to include heat conduction into the model, as has been done in the past (Bandfield and Edwards, 2008; Bandfield, 2009).

The surface slope Gaussian distribution model used here is similar to that described by Helfenstein and Shepard (1999). Rather than modeling individual surface facets, the radiance of each slope and azimuth combination is modeled and its contribution to the measured radiance is weighted by the statistical probability of its occurrence. This reduces the surface slopes and roughness to a single parameter (RMS slope distribution) that is independent of length scales while maintaining reasonable fidelity to natural surfaces. Using the modeled temperatures and slope distributions, the mixture of Planck radiances are calculated in proportion to their contribution to the measurement field of view based on the observation geometry. For example, slopes facing away from the observer will contribute proportionally less to the measurement than slopes facing the observer. This factor is calculated from the scalar product of the vector normal to the surface facet and the observation vector, i.e., from the cosine of the angle between the vectors.

Shadows greatly influence the emitted radiance from planetary surfaces at high angles of solar incidence or where high slope angles are present. There are two aspects to this problem. The first is relatively simple to implement; where the solar incidence for a given slope angle is greater than 90° , the Sun is below the local horizon and the surface temperature is set to 100 K (a lower value should be used for heliocentric distances exceeding 1 AU). In practice, the precise temperature of shaded surfaces matters little for daytime measurements at thermal infrared wavelengths because the amount of radiance is small relative to that from sunlit surfaces.

The second factor is the influence of cast shadows on surfaces that would otherwise be illuminated. We use a shadowing methodology modified from that developed by Smith (1967) and Hapke (1984). This model assumes that any surface element that would otherwise be illuminated has an equal statistical chance of being within a shadow cast by another surface element. This is a relatively simple approach for nadir observations described by the following formula (derived from Eqs. (21) and (24) of Smith, 1967):

$$W(\theta) = \frac{\left[1 - \frac{1}{2} \operatorname{erfc}\left(\frac{\mu}{\sqrt{2}\omega}\right) \right]}{\frac{1}{2} \left[\sqrt{\frac{2}{\pi}} \cdot \frac{\omega}{\mu} e^{-\mu^2/2\omega^2} - \operatorname{erfc}(\mu/\sqrt{2}\omega) \right] + 1}, \quad (17)$$

where $W(\theta)$ is the fraction of the shadowed surface, μ is the cotangent of the solar incidence angle, ω is the RMS surface slope distribution, and $\operatorname{erfc}(x)$ is the error function (the integral between zero and x of a Gaussian distribution function). This equation can only be applied to nadir observations, where no surface is hidden from view (assuming no overhanging surfaces). For off nadir observations, it is necessary to combine Eq. (17) with a function that describes the abundance of cast shadows that are visible from the elevation and azimuth of the viewing platform. For example, when viewing a surface from the same elevation and azimuth as the Sun, no shadowed surfaces will be visible. We will use an approach similar to that described by Hapke (1984). Where the emission angle is greater than the solar incidence angle that shaded fraction observed at nadir, $W_{\text{nadir}}(\theta)$, is modified by the following:

$$W_{\text{view}}(\theta) = W_{\text{nadir}} \cdot \left(1 - e^{-2 \tan(\frac{1}{2}\psi)}\right), \quad (18)$$

where $W_{\text{view}}(\theta)$ is the fraction of shadowing that is present within the field of view. If the emission angle is less than the solar incidence angle, the following applies:

$$W_{\text{view}}(\theta) = W_{\text{nadir}} - W_{\text{obs}}(\theta) \cdot e^{-2 \tan(\frac{1}{2}\psi)}, \quad (19)$$

where $W_{\text{obs}}(\theta)$ is the shadowing function described in Eq. (17), except as applied to the viewing incidence angle of the spacecraft rather than the Sun.

5. Temperature and spectral energy distributions

Due to the complexity of thermal modeling, the number of free parameters is huge and it is impossible to explore the full parameter space in a succinct manner. We here focus on the core problem of this manuscript, i.e., to investigate if the thermal emission properties are sensitive to roughness type. A number of parameters are therefore given constant arbitrary but justifiable values – we fix the heliocentric distance $r_h = 1$ AU, Bond albedo $A = 0$, emissivity $\varepsilon = 1$, conductivity $\kappa = 0$, and consider the spin angular momentum vector to be perpendicular to the orbital plane. If roughness type sensitivity is demonstrated for this parameter set, it is an additional problem to explore how this sensitivity changes character when these parameters are changed.

We consider several different combinations of slope distributions, RMS mean slopes, and wavelengths, for a number of discrete illumination and viewing conditions. It is an unwieldy problem to study a dense grid of $\{i, e, \psi\}$, but a sparse grid is sufficient to demonstrate if and when the roughness type is important.

Section 5.1 describes the properties of the surface temperature distribution itself, which depends on the illumination conditions (i.e., i), but is independent of potential observers (i.e., e and ψ). Section 5.2 describes the spectral energy distributions, and motivates the selection of the illumination and viewing geometries considered.

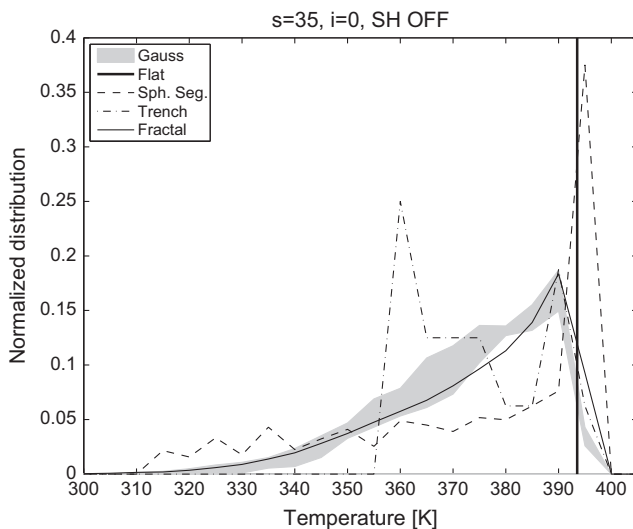


Fig. 5. Histograms of surface temperature in 5 K-wide bins, for $s = 35^\circ$ terrains with topography according to the legend. Illumination is from zenith ($i = 0^\circ$) and there is no self heating (SH OFF). Note that the gray field shows the range of variety for six different realizations of random Gaussian terrains. The distributions are normalized so that bin heights add up to unity.

5.1. Surface temperature distributions

Fig. 5 shows surface temperature histograms for $s = 35^\circ$ and $i = 0^\circ$, i.e., the Sun is at zenith. Here, self heating has been switched off, i.e., the second term on the left hand side of Eq. (14) is ignored. The fraction of emitted radiation that in reality would have been re-absorbed is now artificially removed from the system. Thus, surface temperatures are comparatively low, and essentially only reflect differences in surface slope distributions. The spherical segment surface has a temperature distribution with a strong peak at $T = 393$ K corresponding to flat terrain (slightly displaced from the smooth surface temperature marked by a thick vertical line in Fig. 5 due to the bin size and centers of the histogram), and the largest presence of low temperatures of all terrains, down to $T = 310$ K, due to the unusually steep slopes of the crater rims. The trench terrain has the narrowest temperature distribution, completely lacking $T < 355$ K cases due to the absence of steep slopes. As expected, the temperature distributions of random Gaussian terrains (the shaded region in Fig. 5 shows the range of six different realizations) are similar to that of the fractal terrain (solid curve). The temperature distributions peak at a relatively high temperature, $T = 390$ K, due to the rich presence of facets with $\theta = 10^\circ$ – 30° slopes, not present for trenches or spherical segments.

When self heating is switched on, thermal radiation is allowed to be exchanged between surface elements, leading to higher surface temperatures. Fig. 6 shows temperature distributions calculated with and without self heating. Because our fractal surface model does not have the capacity of calculating self heating, we only show results for spherical segments, trenches, and random Gaussian terrains. However, due to the similarities between random Gaussian terrains and fractals in terms of slope distributions, we suspect that both terrains react similarly to self heating. We also note that the temperature distributions of trenches and random Gaussian terrains are biased towards lower temperatures if the finite terrains considered here are considered representations much larger surfaces, having a similar topography. Facets near

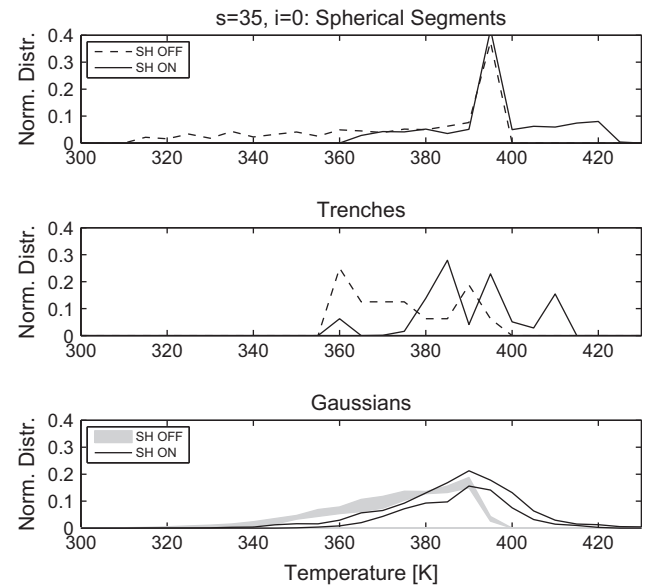


Fig. 6. Histogram of surface temperature in 5 K-wide bins, for $s = 35^\circ$ terrains shaped as spherical segments, sinusoidal trenches and random Gaussians in different panels. Illumination is from zenith ($i = 0^\circ$) and the effect of switching self heating on and off is demonstrated (SH ON/OFF). Note that the gray field shows the range of variety for six different realizations of random Gaussian terrains. The distributions are normalized so that bin heights add up to unity.

the border of the considered domain do not receive diffuse radiation from the exterior, unmodeled, terrain. Spherical segments, if surrounded by flat terrain as in the current work, do not suffer from this limitation due to the strict concavity of the crater geometry. Here, a tilting surface element will always be located within a crater, and is always prevented from seeing facets located outside of the rim – hence, the truncation of the calculational domain does not affect the temperature distribution within the crater. The effect of truncation for partially convex terrains like trenches or Gaussians can be reduced or eliminated by considering a subset of the facets, located deep enough within the modeled terrain to not be influenced by the presence of a boundary (see, e.g., [Davidsson et al., 2013](#)). Although we nominally use the entire terrains when calculating SEDs, tests are being made for subsets to evaluate the sensitivity of SEDs to boundary effects.

With self heating activated, [Fig. 6](#) shows that parts of the rough terrains reach $T = 410\text{--}420\text{ K}$, which is up to $\sim 30\text{ K}$ higher than the subsolar temperature, which is the highest possible temperature of a smooth surface. The self heating also increases the lowest temperatures, raising the minimum value from $\sim 310\text{ K}$ to $\sim 360\text{ K}$. Self heating therefore tends to make the distributions less skewed in the sense that the peak occurs near the center of the temperature range. Most importantly, the temperature distributions are distinctly different for the different terrain types. Spherical segments have a broad flat distribution with a superimposed peak corresponding to the surrounding flat terrain, while the slope distributions of random Gaussian terrains have a triangular shape. Trenches have a rather narrow distribution with three distinct peaks, that in order of increasing temperature, correspond to shallowly illuminated trench walls, sun-facing ridge tops, and valley floors. The latter are hot not only due to small local incidence angles, but also because they are efficiently self heated. The spiky appearance of the temperature distribution therefore does not reflect poor sampling statistics, but the high level of tilt systematics of the terrain.

With increasing solar incidence angle the temperature distributions of the rough surfaces (including self heating) change character. The temperature distribution of spherical segments develops two distinct peaks, while the broad and flat background distribution disappears. The peaks are due to flat isothermal terrain surrounding the crater, and shadowed terrain within the crater, that also obtains an isothermal temperature due to self heating by thermal emission from the illuminated crater wall. The lack of lateral temperature gradients on the shadowed crater interior is a consequence of the geometrical symmetry within a spherical segment – a given facet does not discriminate between nearby or distant facets, and illuminate them identically. Therefore, all facets within the shadow obtain the same self heating flux and reach the same temperature that decreases with increasing solar incidence angle. This is consistent with an analytical solution for the temperature within a spherical segment crater presented by [Lagerros \(1998\)](#), since his Eq. (18) shows that the temperature in the shadow is given by a constant term (for a given i), common to all locations within the crater that are not in direct sunlight. The gradual removal of the broad and flat part of the distribution as i increases is due to the shrinking area of the directly illuminated crater wall, that displays a large variety in temperature. When reaching $i = 80^\circ$, as shown in the lower panel of [Fig. 7](#), only two strong peaks remains of the spherical segment temperature distribution at $T = 195\text{ K}$ (shadow) and $T = 259\text{ K}$ (flat surroundings).

The temperature distribution of self heated sinusoidal trenches maintains its three peaks when i increases, although the peaks broaden and separate. The high-temperature peak corresponds to the directly illuminated trench walls, that can become hot when the Sun is relatively low in the sky with respect to the average ground level, since it is *locally* near zenith. The low-temperature

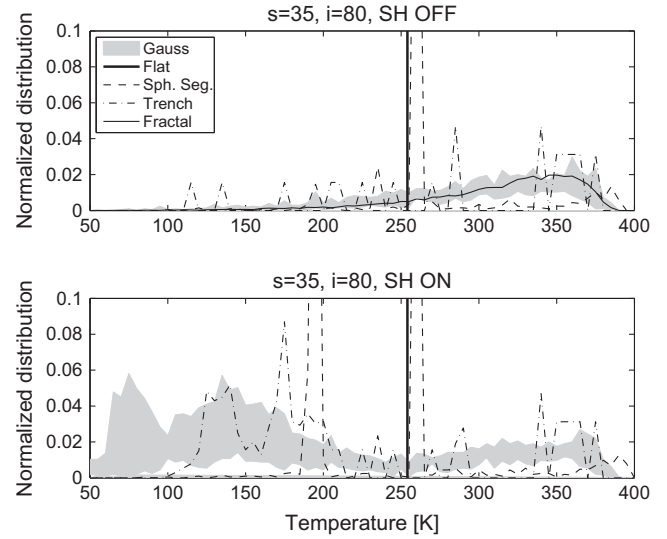


Fig. 7. Histogram of surface temperature in 5 K-wide bins, for $s = 35^\circ$ terrains with topography according to the legend. Illumination is very shallow ($i = 80^\circ$) and self heating is either off (upper panel, SH OFF) or on (lower panel, SH ON). Note that the gray field shows the range of variety for six different realizations of random Gaussian terrains. The distributions are normalized so that bin heights add up to unity.

peak corresponds to the shadowed walls, that only receive energy from the facing sunlit wall. Between these two regions, typically located in the vicinity of ridge tops and valley floors, transition temperatures appear, that causes the intermediate peak. The lower panel of [Fig. 7](#) illustrates conditions at $i = 80^\circ$, with broad peaks at 100–200 K, 220–300 K, and 340–380 K. Thus, a region that would have had $T = 250\text{ K}$ if smooth, locally reaches temperatures up to 400 K due to roughness.

The surface temperature distribution of the self heated random Gaussian terrain is triangular in shape at $i = 0^\circ$, but as the incidence angle increases the peak is shifted from the center to higher temperatures. At the same time, the peak height diminishes, while the low-temperature tail becomes more prominent. At large incidence angles, essentially all temperatures ranging from $\sim 50\text{ K}$ to levels above the subsolar point temperature are represented with similar weights. The lower panel in [Fig. 7](#) shows a broad and essentially flat distribution, where the percentage of cold facets is strongly dependent on the individual characteristics of each terrain.

It is therefore evident that the surface temperature distributions differ systematically between terrains of different types, even when they have the same level of roughness, as measured by parameters like the RMS mean slope s or the Hapke mean slope angle $\bar{\theta}$. We now proceed to study the consequences of this in terms of the thermal emission spectrum, which is one of the observations relevant for remote-sensing instrumentation on spacecraft.

5.2. Spectral energy distributions

The Spectral Energy Distribution (SED) of an unresolved rough terrain will depend strongly on the previously described surface temperature distribution (Section 5.1), that is a function of topography type, level of roughness, solar incidence angle i , and thermo-physical material parameters (we here consider Bond albedo $A = 0$, emissivity $\varepsilon = 1$, and thermal inertia $\Gamma = 0$ for simplicity). However, the viewing geometry of the observer is equally important, since only a fraction of the surface elements may be directly in view, while the remaining elements are hidden behind topographic features. For a given surface temperature distribution on a rough

terrain, the observable SED therefore is also a strong function of emergence angle e and azimuth angle ψ . It is possible that some viewing geometries emphasize and amplify differences, while others tend to minimize the dependence on the exact topography. In the following, three different classes of geometric conditions are considered.

- Case 1: $i = e$ and $\psi = 0^\circ$. These conditions apply for every point on the surface of a body viewed at opposition, if the observer is sufficiently far away from the target. It is particularly relevant for Earth-based observations, where SEDs of this type are needed to build the disk-integrated spectra. However, these conditions may also apply during flyby or distant orbits, although the $i = e$ relation gradually breaks down for regions near the limb, as the distance is decreased. We here focus on the subsolar point ($i = e = 0^\circ$) and a point midway towards the limb ($i = e = 45^\circ$).
- Case 2: $e = 0^\circ$ (for all $\{i, \psi\}$). These conditions apply for orbiting or flyby spacecraft with nadir pointing. Thus, regions under arbitrary illumination conditions are viewed parallel to the local surface normal, which also means that the azimuth angle is unimportant, since the viewing geometry is identical for all ψ when $e = 0^\circ$. We here focus on $i = 0^\circ, 30^\circ, 60^\circ$, and 80° .
- Case 3: arbitrary $\{i, e, \psi\}$. This is the most general geometrical condition for the mapping of a resolved body by spacecraft. We here focus on $i = e = 45^\circ$ and $\psi = 0^\circ, 90^\circ$, and 180° .

5.2.1. Observations at opposition (Case 1)

We consider the subsolar point of a body viewed at opposition. The corresponding surface temperature distributions for the different topographies, when self heating is switched off, are shown in Fig. 5. Based on these distributions, SEDs have been calculated as described in Section 4.2. The result is shown in the upper panel of Fig. 8, which is restricted to $1 \leq \lambda \leq 10 \mu\text{m}$ for clarity. In spite of the large difference between the surface temperature distributions for the different terrains, the resulting SEDs are nearly identical to each other. A substantial difference between temperature distributions is therefore a necessary but not sufficient condition for creating clearly different SEDs. Comparing, e.g., the spherical

segment distribution with the random Gaussian distribution, it is clear that an unusually large area coverage of hot facets can be compensated for by a dearth of medium-temperature facets and an excess of low-temperature facets. At the Planck curve peak, the rough terrains send a radiance towards the observer that is about 21% lower than that of a smooth surface in similar conditions.

When self heating is switched on, the radiances of the rough terrains increase to the level of that of a smooth surface. The spherical segments yield a Planck curve peak radiance that is $\sim 4\%$ higher than that of a smooth surface, while the radiance from the random Gaussian terrain is $\sim 6\%$ weaker than that of the flat surface. Sinusoidal trenches are intermediate between the two. The lower radiances of trenches and random Gaussians may partially be a modeling artifact – if the somewhat cooler boundaries are cut out, modeling shows that the radiance reaches the smooth surface value. The important result in this context is that the beaming effect (near the Planck curve peak) for nadir viewing of the subsolar point is extremely weak, only a few percent, even at a rather high level of roughness. At $s = 5^\circ$ and 20° , the beaming is virtually non-existent. This agrees with previous modeling. For example, Winter and Krupp (1971) found that the best overall fit to the $11 \mu\text{m}$ radiance of the Moon as function of $i = e$ was achieved with spherical segments having $s = 34^\circ$. The modeled subsolar point brightness temperature was $T \approx 385 \text{ K}$, corresponding to a radiance excess of merely 3.5% with respect to a smooth surface with Bond albedo $A = 0.123$ (that has an equilibrium temperature of 381.3 K). Using a similar model, Spencer (1990) favored $s = 39^\circ$, having a subsolar brightness temperature of $T \approx 390 \text{ K}$ and an $11 \mu\text{m}$ excess of 8.2% with respect to a smooth surface. It is worth to point out that both models underestimate the actual measurements of Saari and Shorthill (1972) at $i = e \approx 0^\circ$, which indicated an $11 \mu\text{m}$ brightness temperature of $T = 396.8 \text{ K}$, corresponding to an actual subsolar point radiance excess of the Moon of 10.5–14.9% with respect to a smooth body having $A = 0.08$ – 0.123 . The discrepancy between measurements and models on the $0^\circ \leq i = e \leq 90^\circ$ interval could be due to any combination of roughness variations, albedo and emissivity variations, or inadequacy of the model. In any case, it is clear that it is not the region around the subsolar point that primarily is responsible for the beaming effect seen in disk-integrated emission (e.g., Fig. 2), but it must be the rims. This has also been pointed out by Rozitis and Green (2011).

Conditions change rapidly as $i = e$ increase. At $i = e = 45^\circ$, midway to the limb, a smooth body under lunar conditions would have $T \approx 350 \text{ K}$, while measurements and the previously mentioned models indicate a brightness temperature $T \approx 370$ – 375 K . In this case, the beaming effect is substantially stronger, yielding an $11 \mu\text{m}$ radiance excess of 24–30%. This steady radiance enhancement with increasing $i = e$, with respect to the cosine law expected for a smooth body, is the previously mentioned *limb brightening*. In order to investigate the strength of the beaming predicted by the various topographies, we calculated the SEDs for $i = e = 45^\circ$, as shown in Fig. 9. At $s = 35^\circ$ the Planck curve peak beaming of spherical segments is strong, with a radiance excess of 29.9% with respect to a smooth surface. The random Gaussian terrains have a beaming effect that is only half as strong, and tests show that this is not a boundary artifact. However, the radiance excess of sinusoidal trenches reaches 42–45%, depending on how borders are treated, which is substantially stronger than the beaming of spherical segments.

Simulations with self heating switched off show that the beaming of spherical segments and random Gaussians is primarily caused by self heating. With no self heating accounted for, a fractal surface has a merely 6.9% Planck curve peak radiance excess with respect to a smooth surface, while spherical segments and random Gaussian terrains beam even less. Thus, the redirection of some

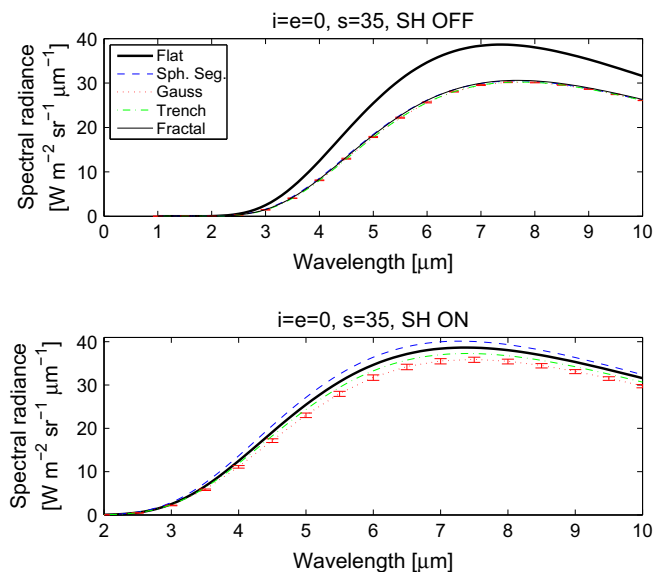


Fig. 8. The 1–10 μm Spectral Energy Distributions (SEDs) for a smooth surface and various rough terrain types with $s = 35^\circ$, with self heating switched off (upper panel, SH OFF) or on (lower panel, SH ON). Illumination is straight from above ($i = 0^\circ$), and nadir-viewing is assumed ($e = 0^\circ$).

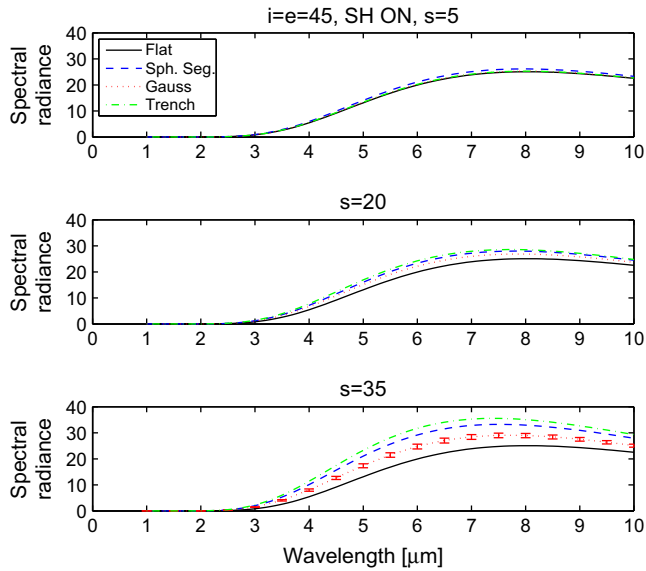


Fig. 9. The 1–10 μm Spectral Energy Distributions (SEDs) with unit $[\text{W m}^{-2} \text{sr}^{-1} \mu\text{m}^{-1}]$ for a smooth surface and various rough terrain types with $s = 5^\circ$ (upper panel), $s = 20^\circ$ (middle panel), and $s = 35^\circ$ (lower panel), with self heating included (SH ON). Illumination and viewing conditions are given by $i = e = 45^\circ$ and $\psi = 0^\circ$. The SED of random Gaussians (dotted) have bars that show the radiance range for six different realizations of the terrain.

facets away from the average normal, and towards the Sun and the observer, is not the main reason for the thermal infrared brightness – it is the boost of surface temperature by self illumination that is responsible. However, this is not the case for sinusoidal trenches. Even with self heating switched off, this terrain has a Planck curve peak radiance excess of 29.9%, almost as large as for spherical segments *with* self heating. The addition of self heating increases the beaming further, to 42–45%. In this case it is therefore primarily the systematic orientation of surface elements towards the Sun and the observer that is responsible for the beaming. A large fraction of the terrain basically acts as a subsolar point.

At $s = 20^\circ$ the emission of trenches is 14.1% stronger than of a smooth surface, but at $s = 5^\circ$ the difference is less than a percent. It is worth pointing out that the relative beaming strengths of the different topographies are similar at all wavelengths – the near-infrared behavior is qualitatively the same as in the thermal infrared.

It is therefore evident that the beaming of atmosphereless body surfaces is topography-dependent. It is not only the level of roughness that is of importance, but the topographic roughness model is important as well.

5.2.2. Nadir-viewing observer (Case 2)

Orbiting spacecraft often use nadir pointing while scanning the surface during mapping. It is therefore important to explore how the different topographies behave under these conditions. Because our main goal is to demonstrate the extent of topography dependence, and because a full parameter comparison would be time consuming, we restrict ourselves to a specific case – a spacecraft flying along the equator of a body with its spin axis perpendicular to the orbit of the body around the Sun, starting at the subsolar point and heading for the terminator.

Fig. 10 shows the SEDs with self heating included, for $s = 35^\circ$ and incidence angles $i = 0^\circ, 30^\circ, 60^\circ$, and 80° in different panels. Due to the geometric restrictions applied here, $e = \psi = 0^\circ$. Note that the upper panel duplicates Fig. 8 for comparative reasons. The beaming effect is weak for $i \lesssim 30^\circ$, as already has been discussed in Section 5.2.1. However, with increasing incidence angle,

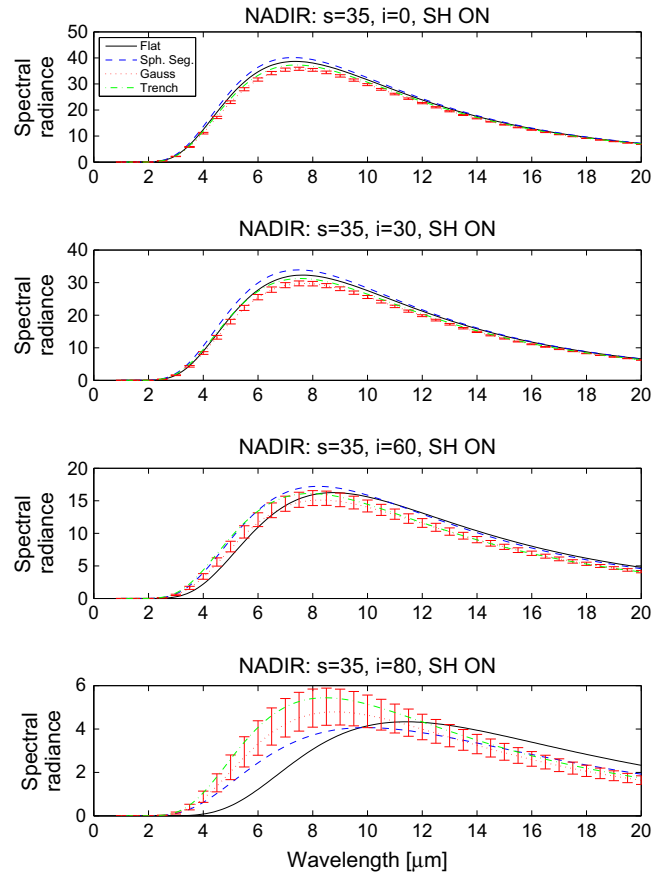


Fig. 10. The 1–20 μm Spectral Energy Distributions (SEDs) with unit $[\text{W m}^{-2} \text{sr}^{-1} \mu\text{m}^{-1}]$ for a smooth surface and various rough terrain types with $s = 35^\circ$, and self heating included (SH ON). The different panels show different incidence angles i , in all cases using emergence angle $e = 0^\circ$, i.e., nadir viewing. The azimuth angle is $\psi = 0^\circ$, i.e., the considered terrain, the Sun and the observer are all in the same plane. The SED of random Gaussians (dotted) have bars that show the radiance range for six different realizations of the terrain.

spherical segments display a beaming effect at short wavelengths, while producing a weaker radiance at long wavelengths compared to the smooth surface. The transition between the two regimes is located in the 8–10 μm region. It is important to point out that this discussion concerns model bodies placed at 1 AU – many Solar System bodies are more distant and cooler, so that the transition occurs at longer wavelengths. We first focus on the short-wavelength regime.

At $i = 60^\circ$, the beaming of the trench surface is as strong as that of spherical segments, and both are located in the upper range of the random Gaussian terrains. However, as the incidence angle grows, the beaming of random Gaussians and sinusoidal trenches rapidly outgrows that of the spherical segments. At $i = 80^\circ$, the $\lambda = 5 \mu\text{m}$ radiance of spherical segments is 3.3 times higher than for a smooth surface, but the corresponding numbers for random Gaussians and trenches are 4.4 and 5.7, respectively. However, the radiance range covered by the six Gaussian realizations is large, in some cases greater than for the trenches, illustrating the strong sensitivity to individual surface characteristics during extremely shallow illumination.

In order to understand this behavior, our simulations with self heating switched off are important. The $\lambda = 5 \mu\text{m}$ radiance of spherical segments, average random Gaussians and trenches are 2.9, 4.2, and 5.6 times higher than that of the smooth surface, respectively. These values are only marginally smaller than the previously mentioned ones, showing that self heating has a weak effect on the SEDs at high incidence angles. This can be understood

by comparing the temperature distributions shown in the upper and lower panels of Fig. 7. The high-temperature part of the distributions is weakly affected by self heating, thus incapable of increasing the already high temperatures. The strongest effect of self heating is to populate the low-temperature part of the distribution, but these facets are still too cold to produce much radiative energy. Therefore, the calculated SEDs depend almost entirely on the facet tilts.

When self heating is ignored, the fractal terrain yields a near-infrared SED that is similar in strength to that of the trenches, and as strong as the SED of the strongest random Gaussian realization. The spherical segments, having a near-infrared SED below that of the faintest random Gaussian realizations, is therefore atypical among the currently considered topographies. This could simply be due to boundary effects – in fact, if boundaries are cut out from the trench and random Gaussians, their SEDs become similar to that of the spherical segment. However, there are reasons to believe that the SEDs shown in Fig. 10 indeed are representative for the range of radiances one can expect for rough terrains. Firstly, the fractal terrain consists of 32,000 facets and is therefore less sensitive to edge effects than the random Gaussians and trenches, that only consist of 2048 facets. In addition, the sunward half was cut out to reduce the small edge effect for the fractal terrain further. We are therefore confident that the fractal terrain provides a true measure of the variety one can expect among SEDs at large i , since these are weakly dependent on self heating. Secondly, the strong reduction in radiance seen for trenches as boundaries are cut out, is primarily due to the loss of a rather steeply inclined leading edge that gets illuminated face-on and thus is hot. Removing the edge is equivalent to adding external topography, that would prevent these particular facets from receiving direct sunlight. However, it would not be difficult to change the trench geometry slightly, in order to maintain the high radiance even when edges are cut out. For example, the trench walls facing the Sun can be made somewhat steeper near the ridge peaks, and the trench walls facing away from the Sun can be made less steep to maintain the same s . Such a “sawtooth” trench terrain would beam strongly at large incidence angles.

Our main point is that spherical segments may not necessarily be very representative of rough terrains at high incidence angles. Its roughness originates from the tilts of the crater interior, but when the Sun is low in the sky only a small fraction of the surface area near the rim is illuminated at locally small incidence angles. These hot regions are solely responsible for the beaming effect, since most of the crater interior is in shadow, only reaching low temperatures driven by self heating, and does not contribute significantly to the beaming. In other words, the spherical segment is inefficient in creating a large area coverage of hot facets at shallow illumination, compared to other topographies. This should be kept in mind when analyzing near-infrared spectroscopic measurements of atmosphereless bodies for poorly illuminated regions.

At wavelengths longer than 8–10 μm the SEDs of rough surfaces are essentially indistinguishable from that of a smooth surface, as long as the incidence angle is small. However, around $i = 60^\circ$ and above, they all yield a *weaker* SED radiance than a smooth surface. At these wavelengths, the fractal terrain SED tends to have the smallest gap to the smooth surface SED, while the other terrains only are slightly fainter and display a fairly good overlap. The spherical segment may therefore be a rather representative terrain type at long wavelengths, in contrast to its end-member behavior in the near-infrared.

5.2.3. Azimuth dependence (Case 3)

During most real observations of a piece of terrain on a resolved body, the incidence plane that contains the terrain average normal

and the Sun, does not coincide with the emergence plane that contains the terrain average normal and the observer, i.e., the azimuth angle is $\psi \neq 0^\circ$. The azimuth angle determines whether the observer primarily sees the sunlit parts of the surface by having the Sun at the back, or the shadowed parts by having the Sun ahead. In order to demonstrate the sensitivity to the azimuth angle for different topographies, we here consider $i = e = 45^\circ$ and $\psi = 0^\circ, 90^\circ$ or 180° . We thus consider the equator of a body having its spin axis perpendicular to the orbital plane, specifically a region being midway between sunrise and noon, on a body with a globally spherical shape. Denote the surface normal of that region by Z , let Y be parallel to the body spin vector, and place X so that a right-handed orthogonal system forms. Using this as a spherical coordinate system to locate the observer, Z is the symmetry axis, the polar angle measured from Z is equivalent to the emergence angle e , while ψ is measured counter-clockwise about Z , starting from X . Thus $\psi = 0^\circ$ is the previously discussed opposition case where sunlit regions dominates the view, $\psi = 90^\circ$ is out of the equatorial plane, looking down on an element lit from the side, while $\psi = 180^\circ$ is an equatorial-plane view of the predominantly shadowed regions.

Fig. 11 shows the 1–20 μm SEDs at the three azimuth angles for rough terrains with $s = 35^\circ$ compared to that of a smooth surface. The $\psi = 0^\circ$ case, extending Fig. 9 coverage to longer wavelengths, displays a strong beaming from rough terrains, as expected when shadows largely are hidden from the field of view by sunlit terrain. However, as the azimuth increases towards $\psi = 90^\circ$ the differences between rough and smooth terrain diminish. The SEDs are similar at all wavelengths, keeping in mind that small absolute differences still could mean large percentile differences at very low radiance levels. As the azimuth increases towards $\psi = 180^\circ$, the SEDs of rough terrains become increasingly fainter, as the field of view becomes dominated by shadowed and cool regions.

The rate by which the radiance changes as ψ increases differs substantially between the topographies. As may be expected by its directional nature, the sinusoidal trenches have the largest change – they have the strongest radiance of all models at $\psi = 0^\circ$, and the weakest radiance of all models at $\psi = 180^\circ$. The

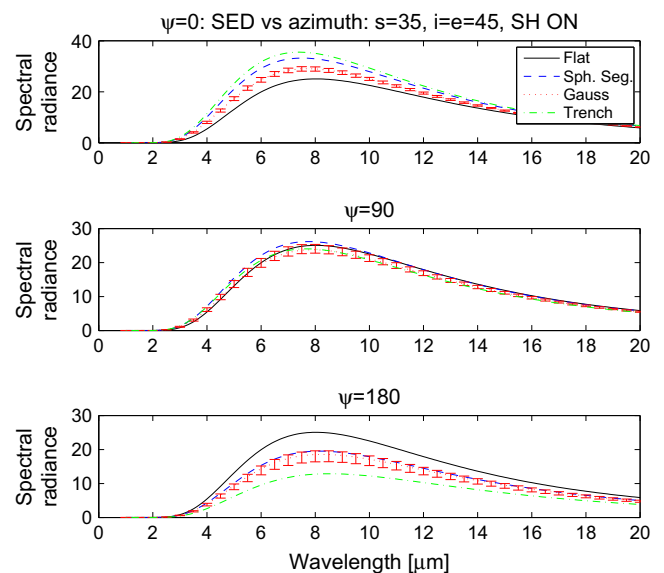


Fig. 11. The 1–20 μm Spectral Energy Distributions (SEDs) with unit $[\text{W m}^{-2} \text{sr}^{-1} \mu\text{m}^{-1}]$ for a smooth surface and various rough terrain types with $s = 35^\circ$, and self heating included (SH ON). In all cases, $i = e = 45^\circ$. The different panels show different azimuth angles $\psi = 0^\circ, 90^\circ$, and 180° . The SED of random Gaussians (dotted) have bars that show the radiance range for six different realizations of the terrain.

random Gaussians have the smallest change, while spherical segments are intermediate.

Simulations with self heating switched off show that spherical segments, random Gaussians, and fractals are similar at all azimuth angles considered. Basically, both spherical segments and fractals fit within the range covered by random Gaussian realizations. The sinusoidal trenches stand out by being much brighter at $\psi = 0^\circ$ and much fainter at $\psi = 180^\circ$ compared to the others. Therefore, it is not the self heating that is the primary source of differences, but the level of alignment versus randomness in surface facet orientations. Highly randomized surfaces like the fractals or random Gaussians always have a fair chance of placing at least a fraction of their facets so that they simultaneously are hot and visible – this reduces the azimuth dependence. A terrain like the trenches, where many facets are co-aligned with each other, facilitates a more extreme angular dependence of the SED.

These few cases further illustrate that the dependence of radiance on roughness cannot be fully described by a single parameter like the RMS mean slope s . The behavior of the SED is more elaborate and sometimes depends strongly on the type of topography in question. This certainly makes the task of retrieving information on resolved Solar System bodies by remote sensing harder. Even if a limited data set can be fit by a model, so that the thermal inertia and level of roughness can be determined, one must remember that these parameters are model-dependent, i.e., depend to a certain extent on the type of topography applied in the model. However, an observational database with a good $\{i, e, \psi\}$ coverage of specific regions, combined with a modeling tool flexible enough to study a large variety of topography types, has the potential of providing unique information regarding the unresolved part of the surface.

6. Realistic versus simplified statistical models

The statistical model described in Section 4.4 was used in order to generate SEDs valid for $s = 5^\circ, 20^\circ$ and 35° for a variety of incidence, emergence and azimuth angles. These models are compared with SEDs calculated for random Gaussian terrains by using the model of Davidsson and Rickman (2014), for the same s and geometric conditions. Note that the borders of the modeled terrain have been disregarded in order to minimize edge effects. Denoting the simplified statistical and thermophysical model SEDs by SED_{stat} and SED_{tpm} , respectively, we consider percentile differences as function of wavelength according to

$$\beta(\lambda) = 100 \frac{SED_{stat} - SED_{tpm}}{SED_{tpm}}. \quad (20)$$

We start by considering an important class of observational geometry for spacecraft missions – the nadir viewing. Fig. 12 shows $\beta(\lambda)$ for $e = 0$. Each panel is valid for a particular level of roughness s and contains four curves corresponding to $i = 0^\circ, 30^\circ, 60^\circ$, and 80° .

We first focus on the bottom panel because many Solar System bodies are as rough as $s = 35^\circ$, corresponding to $\bar{\theta} \approx 25^\circ$ (Cord et al., 2003), and since β can be compared with the range covered by various TPMs, as shown in Fig. 10. As long as $\lambda \geq 5 \mu\text{m}$ and $i \leq 30^\circ$, the differences between SED_{stat} and SED_{tpm} are small, $\beta \leq 2\%$, which is comparable to the spread in radiance for different realizations of random Gaussian models. When the incidence angle increases to $i = 60^\circ$, the simplified statistical model is fainter than SED_{tpm} by about 20%. This is still comparable to differences among TPMs, which is around 20% near the Planck peak, decreasing to $\sim 10\%$ at longer wavelengths. At large incidence angles ($i = 80^\circ$) the radiance from TPMs is sensitive to topography near the Planck peak, but for wavelengths $\lambda \gtrsim 15 \mu\text{m}$ these variations are less than 30%, while $|\beta|$ is twice as large. At near-infrared wave-

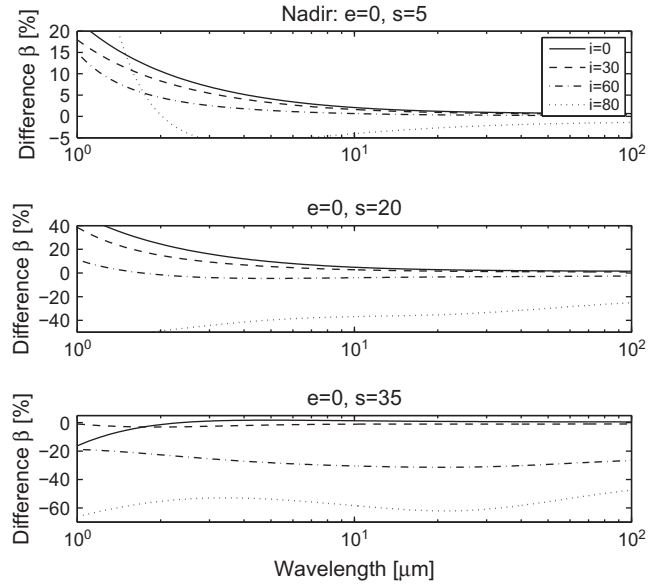


Fig. 12. Percentile difference β between the SEDs of a quasi-analytical model and a full thermophysical model with random Gaussian topography under nadir viewing conditions ($e = 0$), versus incidence angle i and level of roughness s .

lengths ($3 \mu\text{m} \lesssim \lambda \lesssim 5 \mu\text{m}$), and large incidence angles ($i = 80^\circ$), there are substantial differences among TPMs (e.g., 70–80% at $i = 80^\circ$ compared to 10–40% at $i = 40^\circ$). The β -values indicates differences between this particular TPM and the simplified statistical model.

It is therefore evident that, for nadir viewing, the differences between the simplified statistical approach, and a TPM based on random Gaussian topography, are of similar size as the difference between different TPM surface realizations. This is not only the case for a wide range of wavelengths and incidence angles at high roughness, but also applies at $s = 5^\circ$ and $s = 20^\circ$. Thus, surface parameters derived by applying the simplified statistical approach may be biased, but not necessarily more so than for a TPM run for a specific topography type.

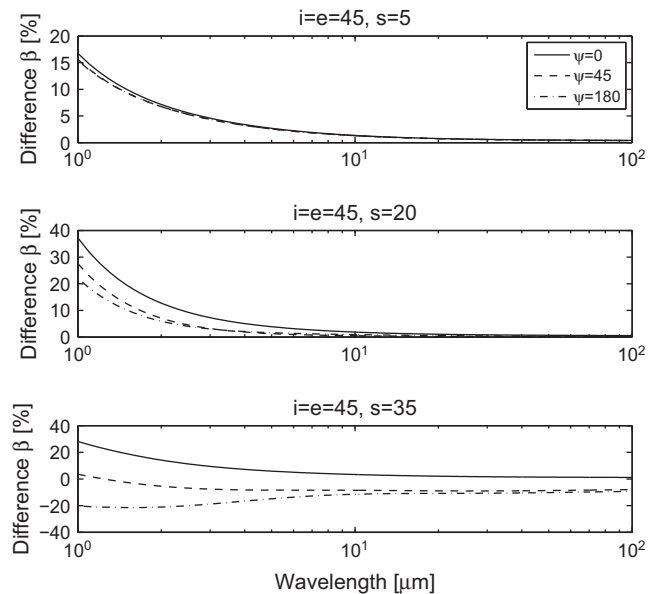


Fig. 13. Percentile difference β between the SEDs of a quasi-analytical model and a full thermophysical model with random Gaussian topography under $i = e = 45^\circ$ conditions, versus azimuth angle ψ and level of roughness s .

In Fig. 13 we show β for a moderate angle of solar incidence ($i = 45^\circ$), viewed off-nadir ($e = 45^\circ$), for different azimuth angles ψ . According to Fig. 11, the thermophysical model radiance near the Planck peak at $\sim 8 \mu\text{m}$ for $s = 35^\circ$ increases by $\sim 100\%$ as the azimuth angle changes from $\psi = 180^\circ$ (shadows fully in view) to $\psi = 0^\circ$ (shadows mostly hidden). This change is large compared to the spread among radiances from random Gaussian surfaces, decreasing from $\sim 20\%$ to 10% . The simplified statistical model shows the same qualitative change with ψ , and remains within $\sim 10\%$ of the corresponding TPM radiance. The similarities between SED_{stat} and SED_{tpm} are maintained at other wavelengths and lower levels of roughness.

It is therefore evident that the simplified statistical approach manages to capture the qualitatively correct behavior of thermal emission and that the errors are not excessive, for a wide variety of wavelengths, roughness levels, illumination and viewing conditions. We emphasize that a TPM is complex to implement and demanding to run since it is physically accurate, while the statistical method is simple and fast at the price of ignoring certain fundamental principles (e.g., energy conservation, by applying approximate corrections for self heating and shadowing). Yet, errors are small enough to justify its application when the usage of a fully implemented TPM is not feasible due to a large amount of data that needs to be analyzed, and/or the time available to perform the analysis is limited.

7. Applications

In order to further illustrate some of the principles discussed in previous sections, we compare here our model calculations with *Deep Impact* data for Comet 9P/Tempel 1 (Groussin et al., 2013) and *LRO* data for the Moon (Paige et al., 2010). Fig. 14 shows the measured $\lambda = 4 \mu\text{m}$ emission of Comet 9P/Tempel 1, divided by the emission expected for a smooth surface in radiative equilibrium, as function of incidence angle i , for near-nadir viewing ($e \leq 12^\circ$). According to Section 3.4 in Davidsson et al. (2013) the radiance of this low- e region is best reproduced with a model having a very rough surface ($\bar{\theta} = 46^\circ$) and a zero thermal inertia, although an upper limit of $I \leq 50$ MKS could not be excluded. In any case, the thermal inertia is sufficiently low to motivate a comparison with a model assuming radiative equilibrium. The flyby did not provide a nadir view of the subsolar point, hence there is no data for small incidence angles. However, the beaming at $52^\circ \leq i \leq 62^\circ$ is weak or non-existent, while the comet emission strength surges relative to a smooth surface at $i > 62^\circ$. This behavior is well reproduced by the models. The models predict little beaming over the entire interval $0 \leq i \leq 60^\circ$, but do predict a limb brightening of the correct order of magnitude at larger incidence angles.

Fig. 15 is a similar plot for the Moon, where much more data is available. The lunar thermal inertia is $I = 50$ MKS but due to the slow rotation of the Moon its thermal parameter (see Spencer et al., 1989) is so low that the Moon is very close to radiative equilibrium, as assumed in our models. We used Diviner Radiometer data (Paige et al., 2010), which measured emitted radiance at all local times from the *LRO* near-polar orbit. The entire $0 \leq i \leq 90^\circ$ region is covered, with $e \leq 3.1^\circ$ everywhere. This produces a dataset with full local time coverage during the day in a manner similar to Vasavada et al. (2012). The $\lambda = 7.8 \mu\text{m}$ radiance (divided by that expected from a smooth surface) has a somewhat peculiar i -dependence. A weak beaming is seen at $i \lesssim 25^\circ$, but at $25^\circ \lesssim i \lesssim 65^\circ$ the lunar emission is fainter than that of a flat surface. At $i \gtrsim 65^\circ$ the beaming returns and quickly becomes very strong. At $i > 80^\circ$, the lunar emission is up to 2.3 times that of a smooth surface (not shown in Fig. 15). The only model providing

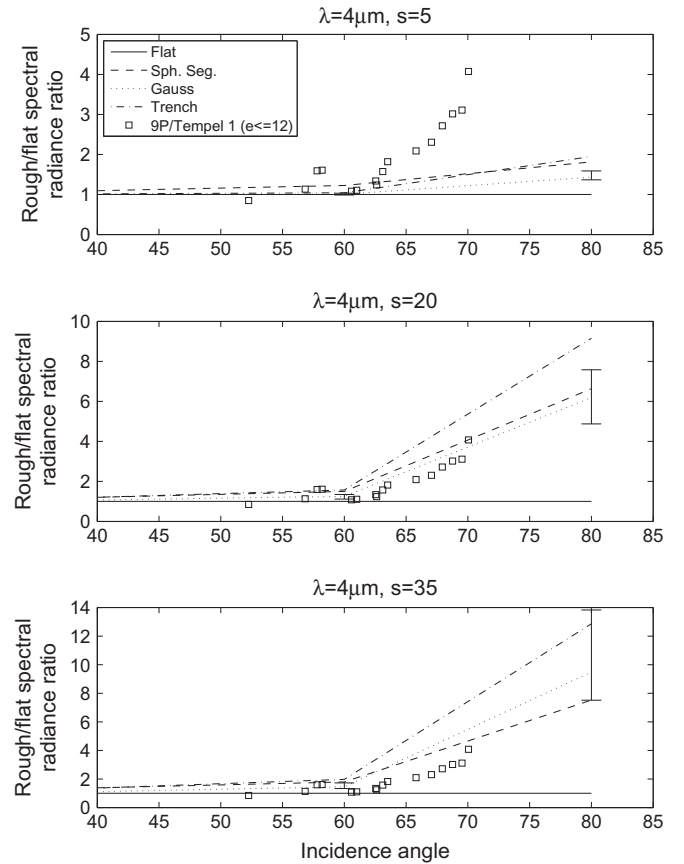


Fig. 14. The $\lambda = 4 \mu\text{m}$ radiance ratio between rough and smooth surface models, versus incidence angle i and level of roughness s , assuming $e = 0$. Overplotted are measured low- e data for Comet 9P/Tempel 1 acquired by *Deep Impact*.

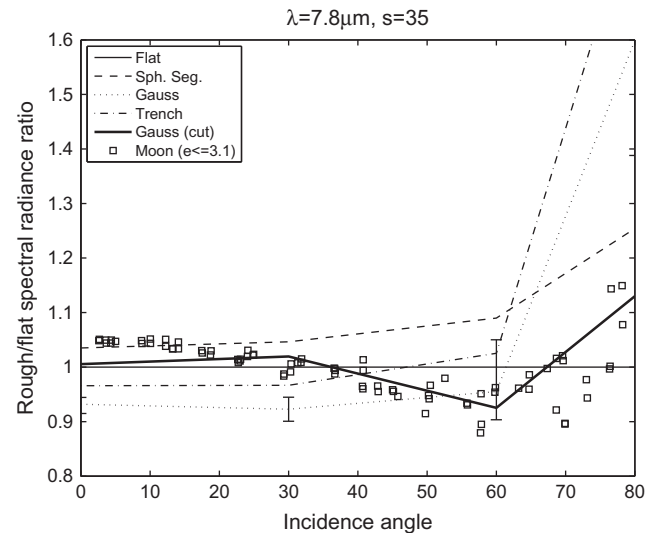


Fig. 15. The $\lambda = 7.8 \mu\text{m}$ radiance ratio between rough ($s = 35^\circ$) and smooth surface models, versus incidence angle i , assuming $e = 0$. Overplotted are measured low- e data for the Moon acquired by the *Lunar Reconnaissance Orbiter* (*LRO*).

a proper $i \lesssim 25^\circ$ beaming is the spherical segments, while edge effects are suppressing the trench and random Gaussian emission. However, if the edges are disregarded (being cooler due to lack of self heating from unmodeled exterior terrain), the random Gaussian surface seen as a thick curve in Fig. 15 more closely matches the data (an even larger simulated terrain, with a more

substantial border cut out, is expected to close the gap entirely). The spherical segments do not capture the decrease in emission at $i \approx 60^\circ$, although we caution that the poor spatial resolution near the crater rim in the model (see Fig. 3) may be partially responsible. However, it is clear that the random Gaussian surface (with edges removed) closely reproduces both the dip at $25^\circ \lesssim i \lesssim 65^\circ$ and the beaming at $i \gtrsim 65^\circ$. The origin of the dip can be seen in the third panel of Fig. 10, where $\lambda = 7.8 \mu\text{m}$ is close to the point where beaming at shorter wavelengths is replaced by an emission deficit at longer wavelengths. The exact transition wavelength depends on i , which means that one may alternate between beaming and a deficit when changing i at a fixed wavelength. Note that the dip is missing in the data for Comet 9P/Tempel 1 because rough terrain always beams at $\lambda = 4 \mu\text{m}$ when the incidence angle is sufficiently large (Fig. 10).

The unmodified random Gaussian and trench surfaces reach radiance ratios of 2.0 and 1.8, respectively, at $i = 80^\circ$, which is close to the most extreme measurement of 2.3 at $i \approx 85^\circ$. The strong beaming of these models is due to unobscured hill sides, which may be present in reality as well. When boundaries are disregarded, directly illuminated hills near the edge no longer contribute to the thermal emission, but are allowed to shadow internal terrain and hide it from view, explaining why the cut random Gaussian does not surge as strongly or as early as the unmodified terrains.

In summary, our models are generally in good agreement with these particular measurements. The LRO Diviner data illustrate the importance of obtaining measurements with a wide range, and high resolution, in illumination and viewing angles, for given surface locations. Obtaining such data sets can be difficult in reality and may require dedicated efforts when planning the spacecraft trajectory and attitude, as well as instrument usage over time. In this particular data set, the measured radiance varies in a non-trivial manner with incidence angle at fixed emergence angle and wavelength. This behavior could roughly be produced with a random Gaussian model, while more modeling efforts are needed to decide whether any of the other roughness types could fit as well. This model diversity – for identical levels of surface roughness s – means that thermal inertia determinations, made while using a specific roughness model, will be biased. If possible, one should therefore apply several different roughness models, to explore the range of uncertainty in thermal inertia estimates.

8. Conclusions: a practical guide for observers

The primary goal of the current work is to investigate whether thermal emission depends on roughness type in addition to roughness level. Our analysis shows that this is the case. For example, when $i = e = 45^\circ$ and $\psi = 0^\circ$ the spherical segments are beaming more strongly than random Gaussian terrains, but weaker than parallel sinusoidal trenches (when oriented as in the current work). When the azimuth angle increases for $i = e = 45^\circ$, the rate by which the emission strength changes is topography-dependent, being strongest for the trenches and weakest for the random Gaussian terrains. Given these initial results, it is likely that disk-integrated radiances will depend on the type of topography as well. Therefore, when a particular topography model is used to interpret observed data, either from ground or in situ, one should acknowledge that the estimated thermal inertia and degree of roughness are model-dependent, at least to a certain extent. Perhaps as importantly, even if it may be impossible to uniquely determine the type of surface roughness from the remote measurements, it is necessary to understand the influence of roughness type used in the model when making comparisons between different observations.

We have not systematically studied the surface slope distributions of all spatially well-resolved Solar System bodies, but, accord-

ing to Section 3.6, both the martian satellite Phobos and the Asteroid (25143) Itokawa have roughness that generally is well-described by the Gaussian functions used by Hapke (1984), on size scales resolved by global shape models. We find that the numerically generated slope statistics of fractals and random Gaussian topographies bear a greater similarity to the real bodies than those of parallel sinusoidal trenches and concave spherical segments. However, we caution that real slope distributions may change character at small spatial scales that remain unresolved by the considered DTMs, and that slope statistics of Solar System bodies may differ systematically with respect to each other, due to the type of surface material and differences in geological evolution.

We have compared a simplified statistical model to a more advanced TPM for a number of illumination and observing geometries, assuming $\Gamma = 0$ in both models. The discrepancies between the two approaches are not always negligible, but of the same order as differences between, e.g., two realizations of random Gaussian terrain, when constructed as described in Section 3.4. Thus, in situations where the usage of more advanced TPMs are not feasible, the simplified statistical method can be applied with a certain degree of confidence.

We emphasize the importance of using thermophysical modeling at specific $\{i, e, \psi\}$ combinations in order to define suitable observing strategies for orbiting spacecraft. Generally, it is difficult to disentangle the effects of thermal inertia, surface roughness level, and topography type. However, the relative strength of these effects depend strongly on illumination and viewing geometry, as well as the considered wavelength region. This makes it possible to plan observations in such a manner that the parameters may be disentangled more easily. In the following we provide practical advice, to be applied in spacecraft mission planning, that will optimize the potential of near- and thermal-infrared instruments. In turn, we discuss the measurement of thermal inertia, degree of roughness, and type of roughness.

8.1. Thermal inertia

In order to determine the thermal inertia of a specific surface region on a resolved body by remote sensing at infrared wavelengths, it is crucial that the region is observed at illumination and viewing conditions for which the effects of roughness are as small as possible. That is to say, the radiance of emitted radiation should essentially be the same, regardless if the surface is flat or very rough. We have indeed found certain combinations of $\{i, e, \psi\}$ and wavelength where the thermal emission is virtually independent of roughness, at least in the $0 \leq s \leq 35^\circ$ range. Although our study was made for $\Gamma = 0$, we do not expect an increased dependence of spectral radiance on roughness for these geometries for non-zero thermal inertia. On the contrary, Rozitis and Green (2011) demonstrated that thermal inertia tends to reduce the beaming effect of terrains with roughness on size scales larger than the skin depth, although their Fig. 6c shows a significant effect remaining at a thermal inertia as high as $\Gamma = 750 \text{ MKS}$. The beaming effect may be removed altogether at large Γ , if roughness only is present on size scales smaller than the thermal skin depth (Davidsson and Rickman, 2014). For these reasons, we do not exclude that there exist geometries other than those discussed here, that also may be suitable for thermal inertia determination (particularly when Γ is large), and we are confident that our current discussion of conditions at specific $\{i, e, \psi\}$ holds also when $\Gamma \neq 0$.

In the following, we also apply a model with $s = 0^\circ$ and $\Gamma \neq 0$. The model solves the 1D heat conduction equation, using a boundary condition for a flat surface that balances the fluxes of solar radiation, thermal re-radiation, and heat conduction. It is used to compare the magnitudes of spectral radiance variation caused by

thermal inertia, with those caused by surface roughness, at specific geometries for which the s -dependence is weak. This is done for illustrative purposes, to demonstrate the potentially strong advantages of observing at these geometries. However, we caution that these results may not be identical to those of a proper TPM with $s \neq 0$ and $\Gamma \neq 0$, although we do not expect our overall conclusions to be affected.

Among the geometries studied here, nadir observations ($e \approx 0^\circ$) of regions to within 30° of the subsolar point (i.e., $i \lesssim 30^\circ$) are particularly well suited for thermal inertia determination when observing near the Planck curve peak ($\lambda = 7.4 \mu\text{m}$ at 1 AU). As we have seen, a high degree of surface roughness ($s = 35^\circ$) will only elevate the radiance by $\leq 4\%$ with respect to a smooth surface. Consider a hypothetical smooth body with rotational period $P = 8 \text{ h}$ and albedo $A = 0.1$, located at $r_h = 1 \text{ AU}$, observed at $\lambda = 7.4 \mu\text{m}$. For a point displaced by 30° from the subsolar point towards the *morning* terminator, the radiance is reduced by 13% when $\Gamma = 50 \text{ MKS}$, and by 26% when $\Gamma = 100 \text{ MKS}$, compared to the case of zero thermal inertia. The $\lambda = 7.4 \mu\text{m}$ radiance for a point displaced 30° from the subsolar point towards the *evening* terminator will be a factor 1.11 higher compared to the forenoon radiance if $\Gamma = 50 \text{ MKS}$, and a factor 1.20 higher if $\Gamma = 100 \text{ MKS}$. Therefore, by observing the same terrain as it passes the subsolar point, strictly maintaining nadir pointing, the influence of roughness is strongly suppressed, and the reduction of radiance versus that of a flat surface with $\Gamma = 0$ and the degree of forenoon/afternoon asymmetry in radiance levels may become powerful tools for determining the thermal inertia. We emphasize that this does not necessarily require the usage of a thermophysical model that includes roughness – if the observed region has a significant thermal inertia, and if the level of surface roughness is not extremely high, a simple model that balances absorbed radiation, thermal re-radiation and heat conduction may suffice.

Additional simulations show that this also holds for heliocentric distances larger than 1 AU. At 3 AU, the beaming elevates the spectral radiance by less than 4% at the Planck curve peak ($\lambda = 12.8 \mu\text{m}$) as long as $i \lesssim 30^\circ$ and $s \lesssim 35^\circ$. A body with $P = 8 \text{ h}$ and $A = 0.1$ at $r_h = 3 \text{ AU}$ has a $i = 30^\circ$ forenoon $12.8 \mu\text{m}$ spectral radiance reduction of 13%, 46% and 62% with respect to a surface with zero thermal inertia if $\Gamma = 10 \text{ MKS}$, 50 MKS, and 100 MKS, respectively. The corresponding ratios of afternoon and forenoon $i = 30^\circ$ radiances are 1.1, 1.5, and 1.7, respectively.

Incidence angles higher than $\sim 30^\circ$ should be avoided. When $i \neq 0^\circ$, it is also very dangerous to consider emergence angles larger than zero, since surface roughness rapidly starts to have a strong effect on the emission. Surface roughness can either act to enhance the emission, or to reduce it, depending on the viewing geometry, making it virtually impossible to determine the thermal inertia in a reliable manner. However, there are possible exceptions to this rule, which could be exploited in order to estimate the thermal inertia for regions that never experience $i \lesssim 30^\circ$ during rotation. Our simulations indicate that the dependence on roughness is very small when $e \approx i$ and $\psi \approx 90^\circ$. We have only verified this for $e = i = 45^\circ$. Therefore, an important topic for future work is to explore how the critical ψ -value changes with $e = i$, and whether $e \neq i$ is possible.

At short wavelengths (e.g., $\lambda = 4 \mu\text{m}$) the beaming due to roughness is somewhat stronger than at the Planck curve peak. For $i = 0^\circ$ and $s \lesssim 35^\circ$, a concave spherical segment model yields $\leq 9\%$ higher radiance than a smooth surface at $r_h = 1 \text{ AU}$, increasing to $\leq 17\%$ and $\leq 24\%$ at $r_h = 2 \text{ AU}$ and $r_h = 3 \text{ AU}$, respectively. Although the incidence angle can increase to 30° at $r_h = 1 \text{ AU}$ without changing the degree of nadir beaming by more than $\sim 5\%$, this window shrinks to $i \lesssim 15\text{--}20^\circ$ at $r_h = 2\text{--}3 \text{ AU}$. Determination of the thermal inertia thus becomes harder and more uncertain, particularly when $\Gamma \lesssim 50 \text{ MKS}$. For example, a terrain with $s = 35^\circ$

and $\Gamma = 50 \text{ MKS}$ have canceling beaming and thermal inertia effects at $r_h = 1 \text{ AU}$. Therefore, its spectral radiance at $i = 0^\circ$ is indistinguishable from that of a smooth surface with zero thermal inertia. Any sign of pre- and post-noon radiance asymmetry is thus crucially important in order to distinguish between these possibilities. Conditions improve somewhat at larger heliocentric distances. Although the beaming effect is stronger (e.g., $\leq 17\%$ beaming effect for $s \lesssim 35^\circ$ at $r_h = 2 \text{ AU}$), the thermal inertia effect is stronger as well (reducing the $i = e = 0^\circ$ radiance by 42% and 65% when $\Gamma = 50 \text{ MKS}$ and $\Gamma = 100 \text{ MKS}$, respectively).

As pointed out by Ekkehard Kürt (2014, personal communication), the subsolar-point beaming seen at short wavelengths during nadir viewing, can be reduced substantially by increasing the emergence angle. Our simulations with concave spherical segments and random Gaussian models confirm that roughness effects disappear near $e \approx 60^\circ$ when $i = 0^\circ$ and $\lambda = 4 \mu\text{m}$. However, the spectral radiance of a rough surface is changing rapidly with emergence angle around $e \approx 60^\circ$ (e.g., for $r_h = 2 \text{ AU}$ and $s = 35^\circ$ the radiance is 4% higher at $e = 50^\circ$ but 22% lower at $e = 70^\circ$, compared to that of a smooth surface). Therefore, a $\pm 10^\circ$ uncertainty in the orientation of the average outward surface normal means a substantial uncertainty in the radiance. At emergence angles as high as $e \approx 60^\circ$, a $\pm 10^\circ$ uncertainty for the incidence angle may also introduce unwanted ψ -dependent effects. Thus, it can be difficult to know if a considered e -value indeed corresponds to the critical value where roughness effects disappear. As an illustration of this problem, Davidsson et al. (2013) analyzed the $\lambda = 4.4 \mu\text{m}$ spectral radiance of the subsolar point ($i = 0^\circ$) of Comet 9P/Tempel 1, as measured by *Deep Impact* at an emergence angle of 63° (both angles are subjected to uncertainties of $5^\circ\text{--}10^\circ$). As seen in Fig. 9 in that paper, the spectral radiance is indeed weakly dependent on roughness – an increase in the level of roughness from zero to $\bar{\theta} = 46^\circ$ led to a 15% reduction of the model spectral radiance. As a result, the thermal inertia at the subsolar point was estimated to be $\Gamma = 200 \text{ MKS}$ in the event that the unresolved surface was smooth, but $\Gamma = 150 \text{ MKS}$ if it was rough. Perhaps this estimate could have been tested more rigorously and further constrained, had nadir observations of the $i \lesssim 30^\circ$ region been available.

These advice apply for observations of the sunlit part of a body. Infrared instruments with sufficient sensitivity can also observe emission from the nightside, and determine the thermal inertia from the rate of cooling. It is out of scope to here discuss the effect of surface roughness on night-time emission.

8.2. Degree of roughness

In order to accurately measure the degree of roughness, it is necessary that the thermal inertia of the region is already known, and that an illumination and viewing geometry is selected, for which the sensitivity to roughness type is weak, but the dependence on degree of roughness is strong. From our simulations, these conditions are met for nadir viewing ($e \approx 0$) of regions that are illuminated at very high incidence ($i \approx 80^\circ$). However, the Planck curve peak should be avoided, and one needs to use shorter or longer wavelengths – this is where a significant difference between flat and rough terrains are seen and our different roughness types yield similar results. As an example (bottom panel of Fig. 10), a flat surface would emit a radiance of $\sim 0.1 \text{ W m}^{-2} \text{ sr}^{-1} \mu\text{m}^{-1}$ at $\lambda = 4 \mu\text{m}$. All our rough models with $s = 20^\circ$ yield the radiance $0.4\text{--}0.6 \text{ W m}^{-2} \text{ sr}^{-1} \mu\text{m}^{-1}$, while the $s = 35^\circ$ models cluster at $0.6\text{--}1.0 \text{ W m}^{-2} \text{ sr}^{-1} \mu\text{m}^{-1}$. If we instead consider the long-wavelength tail, e.g., at $\lambda = 20 \mu\text{m}$, a flat surface would emit $2.3 \text{ W m}^{-2} \text{ sr}^{-1} \mu\text{m}^{-1}$, while all considered rough terrains are fainter, e.g., $1.6\text{--}2.1 \text{ W m}^{-2} \text{ sr}^{-1} \mu\text{m}^{-1}$ at $s = 20^\circ$. However, for $s = 35^\circ$ the radiances are $1.5\text{--}2.0 \text{ W m}^{-2} \text{ sr}^{-1} \mu\text{m}^{-1}$, i.e., indistinguishable from those of $s = 20^\circ$. Hence, the short

wavelength tail appears better suited for determining the level of roughness s , while observations at long wavelengths can confirm that the surface is rough, but not to what level.

8.3. Type of roughness

If the thermal inertia and level of roughness have been estimated for a particular region, one may also attempt to investigate the type of roughness. Our simulations for $i = e = 45^\circ$ show that the difference in radiance between $\psi = 0^\circ$ and $\psi = 180^\circ$ observations is substantial, and appears to increase with the degree of order on the surface (Fig. 11). For example, spherical segments give rise to a larger fluctuation than random Gaussian terrain. It may therefore be possible to distinguish if an unresolved piece of terrain is dominated by a crater with a size comparable to the terrain itself, or consists of a random collection of smaller hills and pits that sit on a quasi-flat background topography. In case the terrain consists of series of parallel trenches, e.g., grooves or cracks formed by various forms of stress, such terrain could exhibit a particularly strong ψ -dependence of emission, as long as the trenches are roughly perpendicular to the incidence plane.

We therefore conclude that near- and thermal-infrared observations of atmosphereless Solar System bodies by spacecraft have a high potential of retrieving information on the thermal inertia, degree of roughness and statistical properties of small-scale topography. However, requirements for thermophysical modeling are high, and it is clear that special observational strategies are needed in order to disentangle thermal inertia, level of roughness and type of topography. We have here demonstrated that the choice of surface topography in thermophysical models is non-trivial. We have also illustrated that systematic simulations, where the $\{i, e, \psi\}$ phase space is investigated, for different values of roughness level s , roughness type and wavelength, provides the background information needed to define suitable observational strategies.

In a follow-up paper, we will focus on the problem of how to break the degeneracy between thermal inertia and surface roughness in thermal disk-integrated measurements. This is done by considering two thoroughly observed objects with well known shapes, sizes and spin-properties; (1) the high- I Asteroid (25143) Itokawa, for which thermal observations are available that cover a wide range of pre- and post-opposition phase angles; (2) the low- I Asteroid (21) Lutetia. Specifically, we use an advanced TPM to systematically explore the parameter space and compare observed and modeled properties, to isolate conditions under which the coupling between thermal inertia and surface roughness safely can be disentangled, and the two parameters individually determined.

Acknowledgments

The authors gratefully acknowledge the financial support and hospitality of the International Space Science Institute (ISSI) in Bern, Switzerland, which made this work possible by sponsoring and hosting our “ISSI-team” meetings during 2011–2014. Davidsson also wishes to thank the Swedish National Space Board (SNSB) for financing contract 102/12. Rickman and Wilska were supported by Grant Nr. 791/N-ROSJA/2010/0 of the Polish National Science Centre.

References

Bandfield, J.L., 2009. Effects of surface roughness and graybody emissivity on martian thermal infrared spectra. *Icarus* 202, 414–428.
 Bandfield, J.L., Edwards, C.S., 2008. Derivation of martian surface slope characteristics from directional thermal infrared radiometry. *Icarus* 193, 139–157.

Barnsley, M.F. et al., 1988. *The Science of Fractal Images*. Springer-Verlag, New York, USA.
 Besse, S. et al., 2014. Lutetia's lineaments. *Planet. Space Sci.* 101, 186–195.
 Bowell, E. et al., 1989. Application of photometric models to asteroids. In: Binzel, R.P., Gehrels, T., Matthews, M.S. (Eds.), *Asteroids II*. The University of Arizona Press, Tucson, pp. 524–556.
 Buhl, D., Welch, W.J., Rea, D.G., 1968a. Reradiation and thermal emission from illuminated craters on the lunar surface. *J. Geophys. Res.* 73 (16), 5281–5295.
 Buhl, D., Welch, W.J., Rea, D.G., 1968b. Anomalous cooling of a cratered lunar surface. *J. Geophys. Res.* 73 (24), 7593–7608.
 Capria, M.T. et al., 2014. Vesta surface thermal properties map. *Geophys. Res. Lett.* 41 (5), 1438–1443.
 Cheng, A.F. et al., 2002. Small-scale topography of 433 Eros from laser altimetry and imaging. *Icarus* 155 (1), 51–74.
 Cord, A.M. et al., 2003. Planetary regolith surface analogs: optimized determination of Hapke parameters using multi-angular spectro-imaging laboratory data. *Icarus* 165, 414–427.
 Davidsson, B.J.R., Rickman, H., 2014. Surface roughness and three-dimensional heat conduction in thermophysical models. *Icarus* 243, 58–77.
 Davidsson, B.J.R., Gutiérrez, P.J., Rickman, H., 2009. Physical properties of morphological units on Comet 9P/Tempel 1 derived from near-IR Deep Impacts spectra. *Icarus* 201, 335–357.
 Davidsson, B.J.R. et al., 2013. Thermal inertia and surface roughness of Comet 9P/Tempel 1. *Icarus* 224, 154–171.
 Delbò, M., Tanga, P., 2009. Thermal inertia of main belt asteroids smaller than 100 km from IRAS data. *Planet. Space Sci.* 57, 259–265.
 Delbò, M. et al., 2007. Thermal inertia of near-Earth asteroids and implications for the magnitude of the Yarkovsky effect. *Icarus* 190, 236–249.
 Denevi, B.W. et al., 2013. The distribution and origin of smooth plains on Mercury. *J. Geophys. Res.* 118, 891–907.
 Emery, J.P. et al., 1998. Mercury: Thermal modeling and mid-infrared (5–12 μm) observations. *Icarus* 136, 104–123.
 Gaskell, R.W., 2011. Gaskell Phobos Shape Model V1.0. VO1-SA-VISA/VISB-5-PHOBOSHAPE-V1.0. NASA Planetary Data System.
 Gaskell, R., et al., 2008. Gaskell Itokawa Shape Model V1.0. HAY-A-AMICA-5-ITOKAWASHAPE-V1.0. NASA Planetary Data System.
 Giese, B., Kürt, E., 1990. Theoretical interpretation of infrared measurements at Deimos in the framework of crater radiation. *Icarus* 88, 372–379.
 Groussin, O. et al., 2013. The temperature, thermal inertia, roughness and color of the nuclei of Comets 103P/Hartley 2 and 9P/Tempel 1. *Icarus* 222, 580–594.
 Gutiérrez, P.J. et al., 2001. Effects of irregular shape and topography in thermophysical models of heterogeneous cometary nuclei. *Astron. Astrophys.* 374, 326–336.
 Hansen, O.L., 1977. An explication of the radionetric method for size and albedo determination. *Icarus* 31, 456–482.
 Hapke, B., 1984. Bidirectional reflectance spectroscopy. 3. Correction for macroscopic roughness. *Icarus* 59, 41–59.
 Hapke, B., 1993. *Theory of Reflectance and Emittance Spectroscopy*. Cambridge University Press.
 Harris, A.W. et al., 2005. The surface properties of small asteroids: Peculiar Betulia – A case study. *Icarus* 179, 95–108.
 Helfenstein, P., Shepard, M.K., 1999. Submillimeter-scale topography of the lunar regolith. *Icarus* 141, 107–131.
 Howett, C.J.A. et al., 2010. Thermal inertia and bolometric Bond albedo values for Mimas, Enceladus, Thethys, Dione, Rhea and Iapetus as derived from Cassini/CIRS measurements. *Icarus* 206 (2), 573–593.
 Keihm, S. et al., 2010. Interpretation of combined infrared, submillimeter, and millimeter thermal flux data obtained during the Rosetta fly-by of Asteroid (21) Lutetia. *Icarus* 221 (1), 395–404.
 Kürt, E. et al., 1992. Interpretation of the KRFM-infrared measurements of Phobos. *Icarus* 96, 213–218.
 Lagerros, J.S.V., 1996. Thermal physics of asteroids. I. Effects of shape, heat conduction and beaming. *Astron. Astrophys.* 310, 1011–1020.
 Lagerros, J.S.V., 1997. Thermal physics of asteroids. III. Irregular shapes and albedo variations. *Astron. Astrophys.* 325, 1226–1236.
 Lagerros, J.S.V., 1998. Thermal physics of asteroids. IV. Thermal infrared beaming. *Astron. Astrophys.* 332, 1123–1132.
 Lauretta, D.S. The OSIRIS-REx team, 2012. An overview of the OSIRIS-REx asteroid sample return mission. *Lunar Planet. Sci. Conf.* 43, 2491.
 Leyrat, C. et al., 2011. Thermal properties of the Asteroid (2867) Steins as observed by VIRTIS/Rosetta. *Astron. Astrophys.* 531, Article ID A168.
 Masiero, J.R. et al., 2014. Main-belt asteroids with WISE/NEOWISE: Near-infrared albedos. *Astrophys. J.* 791 (2), Article ID 121.
 Mueller, M., 2007. *Surface Properties of Asteroids from Mid-Infrared Observations and Thermophysical Modeling*. Universitätsbibliothek der Freien Universität Berlin, Berlin. PhD Thesis. <http://www.diss.fu-berlin.de/diss/receive/FUDISS_thesis_000000002596>.
 Müller, T.G., Blommaert, J.A.D.L., 2004. 65 Cybele in the thermal infrared: Multiple observations and thermophysical analysis. *Astron. Astrophys.* 418, 347–356.
 Müller, T.G. et al., 2005. Thermal infrared observations of the Hayabusa spacecraft target Asteroid 25143 Itokawa. *Astron. Astrophys.* 443 (1), 347–355.
 Okada, T. et al., 2014. Thermal-infrared imaging of C-class Asteroid 162173 (1999 JU₃) by Hayabusa-2. *Lunar Planet. Sci. Conf.* 45, 1201.
 Özisik, M.N., 1985. *Heat transfer. A Basic Approach*. McGraw-Hill, Inc., New York.
 Paige, D.A. et al., 2010. The lunar reconnaissance orbiter diviner lunar radiometer experiment. *Space Sci. Rev.* 150, 125–160.

- Pettit, E., Nicholson, S.B., 1930. Lunar radiation and temperatures. *Astrophys. J.* 71, 102–135.
- Prockter, L.M. et al., 2010. Characteristics of icy surfaces. *Space Sci. Rev.* 153, 63–111.
- Rozitis, B., Green, S.F., 2011. Directional characteristics of thermal-infrared beaming from atmosphereless planetary surfaces – A new thermophysical model. *Mon. Not. R. Astron. Soc.* 415, 2042–2062.
- Saari, J.M., Shorthill, R.W., 1963. Isotherms of crater regions on the illuminated and eclipsed Moon. *Icarus* 2, 115–136.
- Saari, J.M., Shorthill, R.W., 1972. The sunlit lunar surface. I. Albedo studies and full Moon temperature distribution. *The Moon* 5, 161–178.
- Saupe, D., 1991. Random fractals in image synthesis. In: Crilly, J., Earnshaw, R.A., Jones, H. (Eds.), *Fractals and Chaos*. Springer-Verlag, New York, USA, pp. 89–118.
- Smith, B.G., 1967. Lunar surface roughness: Shadowing and thermal emission. *J. Geophys. Res.* 72, 4059–4067.
- Spencer, J.R., 1990. A rough-surface thermophysical model for airless planets. *Icarus* 83, 27–38.
- Spencer, J.R., Lebofsky, L.A., Sykes, M.V., 1989. Systematic biases in radiometric diameter determinations. *Icarus* 78, 337–354.
- Stansberry, J.A. et al., 2012. Physical properties of trans-neptunian binaries (120347) Salacia–Actaea and (42355) Typhon–Echidna. *Icarus* 219, 676–688.
- Thomas, P. et al., 1979. Grooves on Phobos: Their distribution, morphology and possible origin. *J. Geophys. Res.* 84 (B14), 8457–8477.
- Trilling, D.E. et al., 2010. ExploreNEOs. I. Description and first results from the Warm Spitzer Near-Earth Object Survey. *Astron. J.* 140 (3), 770–784.
- Vasavada, A.R. et al., 2012. Lunar equatorial surface temperatures and regolith properties from the Diviner Lunar Radiometer Experiment. *J. Geophys. Res.* 117, Article ID E00H18.
- Winter, D.F., Krupp, J.A., 1971. Directional characteristics of infrared emission from the Moon. *The Moon* 2, 279–292.